



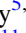


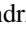
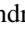
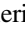


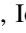
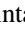
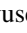


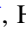
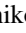
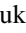
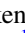
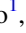
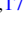


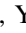




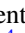



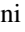
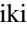








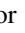


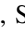


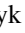


OGLE-2019-BLG-0825: Constraints on the Source System and Effect on Binary-lens Parameters Arising from a Five-day Xallarap Effect in a Candidate Planetary Microlensing Event

Yuki K. Satoh^{1,2,46} , Naoki Koshimoto^{1,46} , David P. Bennett^{3,4,46} , Takahiro Sumi^{1,46} , Nicholas J. Rattenbury^{5,46} ,
Daisuke Suzuki^{1,46} , Shota Miyazaki^{6,46} , Ian A. Bond^{7,46} , Andrzej Udalski^{8,47} , Andrew Gould^{9,10,48} , Valerio Bozza^{11,12,49} ,
Martin Dominik^{13,49} , Yuki Hirao^{45,46} , Iona Kondo^{1,46} , Rintaro Kirikawa^{1,46} , Ryusei Hamada¹





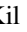
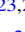

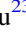




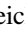

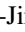





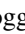
(Leading Authors),

Fumio Abe¹⁴ , Richard Barry³ , Aparna Bhattacharya^{3,4} , Hirosane Fujii¹ , Akihiko Fukui^{15,16} , Katsuki Fujita¹ , Tomoya Ikeno¹ ,
Stela Ishitani Silva^{3,17} , Yoshitaka Itow¹⁴ , Yutaka Matsubara¹⁴ , Sho Matsumoto¹ , Yasushi Muraki¹⁴ , Kosuke Niwa¹ ,
Arisa Okamura¹ , Greg Olmschenk³ , Clément Ranc¹⁸ , Taiga Toda¹ , Mio Tomoyoshi¹ , Paul J. Tristram¹⁹ ,
Aikaterini Vandorou^{3,4} , Hibiki Yama¹ , Kansuke Yamashita¹

(The MOA Collaboration),


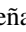
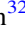



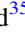
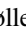






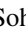

Przemek Mróz⁸ , Radosław Poleski⁸ , Jan Skowron⁸ , Michał K. Szymański⁸ , Radek Poleski⁸ , Igor Soszyński⁸ ,
Paweł Pietrukowicz⁸ , Szymon Kozłowski⁸ , Krzysztof Ulaczyk²⁰ , Krzysztof A. Rybicki^{8,21} , Patryk Iwanek⁸ ,
Marcin Wrona⁸ , Mariusz Gromadzki⁸ 

(The OGLE Collaboration),

Michael D. Albrow²² , Sun-Ju Chung²³ , Cheongho Han²⁴ , Kyu-Ha Hwang²³ , Doeon Kim²⁴ , Youn Kil Jung^{23,25} ,
Hyoun Woo Kim²³ , Yoon-Hyun Ryu²³ , In-Gu Shin²⁶ , Yossi Shvartzvald²¹ , Hongjing Yang²⁷ , Jennifer C. Yee²⁶ ,
Weicheng Zang²⁷ , Sang-Mok Cha^{23,28} , Dong-Jin Kim²³ , Seung-Lee Kim²³ , Chung-Uk Lee²³ , Dong-Joo Lee²³ ,
Yongseok Lee^{23,28} , Byeong-Gon Park^{23,25} , Richard W. Pogge²⁹ 

(The KMTNet Collaboration),

and

Uffe G. Jørgensen³⁰ , Penélope Longa-Peña³¹ , Sedighe Sajadian³² , Jesper Skottfelt³³ , Colin Snodgrass³⁴ ,
Jeremy Tregloan-Reed³⁵ , Nanna Bach-Møller³⁶ , Martin Burgdorf³⁷ , Giuseppe D'Agò³⁸ , Lauri Haikala³⁹ ,
James Hitchcock¹³ , Markus Hundertmark⁴⁰ , Elaha Khalouei⁴¹ , Nuno Peixinho⁴² , Sohrab Rahvar⁴³ ,
John Southworth⁴⁴ , and Petros Spyrtos⁴⁴

(The MiNDSTeP Collaboration)

¹ Department of Earth and Space Science, Graduate School of Science, Osaka University, 1-1 Machikaneyama-cho, Toyonaka, Osaka 560-0043, Japan; satohyk@iral.ess.sci.osaka-u.ac.jp

² College of Science and Engineering, Kanto Gakuin University, 1-50-1 Mutsuurahigashi, Kanazawa-ku, Yokohama, Kanagawa 236-8501, Japan
³ Code 667, NASA Goddard Space Flight Center, Greenbelt, MD 20771, USA

⁴ Department of Astronomy, University of Maryland, College Park, MD 20742, USA

⁵ Department of Physics, University of Auckland, Private Bag 92019, Auckland, New Zealand

⁶ Institute of Space and Astronautical Science, Japan Aerospace Exploration Agency, Kanagawa 252-5210, Japan

⁷ Institute of Natural and Mathematical Sciences, Massey University, Auckland 0745, New Zealand

⁸ Astronomical Observatory, University of Warsaw, Al. Ujazdowskie 4, 00-478 Warszawa, Poland

⁹ Max Planck Institute for Astronomy, Königstuhl 17, D-69117, Heidelberg, Germany

¹⁰ Department of Astronomy, Ohio State University, 140 W. 18th Avenue, Columbus, OH 43210, USA

¹¹ Dipartimento di Fisica “E.R. Caianiello,” Università di Salerno, Via Giovanni Paolo II 132, I-84084 Fisciano, Italy

¹² Istituto Nazionale di Fisica Nucleare, Sezione di Napoli, Napoli, Italy

¹³ University of St Andrews, Centre for Exoplanet Science, SUPA School of Physics & Astronomy, North Haugh, St Andrews KY16 9SS, UK

¹⁴ Institute for Space–Earth Environmental Research, Nagoya University, Nagoya 464-8601, Japan

¹⁵ Department of Earth and Planetary Science, Graduate School of Science, The University of Tokyo, 7-3-1 Hongo, Bunkyo-ku, Tokyo 113-0033, Japan

¹⁶ Instituto de Astrofísica de Canarias, Vía Láctea s/n, E-38205 La Laguna, Tenerife, Spain

¹⁷ Department of Physics, The Catholic University of America, Washington, DC 20064, USA

¹⁸ Sorbonne Université, CNRS, UMR 7095, Institut d’Astrophysique de Paris, 98 bis bd Arago, F-75014 Paris, France

¹⁹ University of Canterbury Mt. John Observatory, P.O. Box 56, Lake Tekapo 8770, New Zealand

²⁰ Department of Physics, University of Warwick, Gibbet Hill Road, Coventry CV4 7AL, UK

²¹ Department of Particle Physics and Astrophysics, Weizmann Institute of Science, Rehovot 76100, Israel

²² University of Canterbury, Department of Physics and Astronomy, Private Bag 4800, Christchurch 8020, New Zealand

²³ Korea Astronomy and Space Science Institute, Daejeon 34055, Republic of Korea

²⁴ Department of Physics, Chungbuk National University, Cheongju 28644, Republic of Korea

²⁵ University of Science and Technology, Korea, (UST), 217 Gajeong-ro, Yuseong-gu, Daejeon 34113, Republic of Korea

²⁶ Center for Astrophysics | Harvard & Smithsonian, 60 Garden Street, Cambridge, MA 02138, USA

²⁷ Department of Astronomy and Tsinghua Centre for Astrophysics, Tsinghua University, Beijing 100084, People’s Republic of China

²⁸ School of Space Research, Kyung Hee University, Yongin, Gyeonggi 17104, Republic of Korea

²⁹ Department of Astronomy, The Ohio State University, 140 W. 18th Avenue, Columbus, OH 43210, USA

³⁰ Centre for ExoLife Sciences, Niels Bohr Institute, University of Copenhagen, Øster Voldgade 5, DK-1350 Copenhagen, Denmark

³¹ Centro de Astronomía, Universidad de Antofagasta, Avenida Angamos 601, Antofagasta 1270300, Chile

³² Department of Physics, Isfahan University of Technology, Isfahan 84156-83111, Iran

³³ Centre for Electronic Imaging, Department of Physical Sciences, The Open University, Milton Keynes MK7 6AA, UK

³⁴ Institute for Astronomy, University of Edinburgh, Royal Observatory, Edinburgh EH9 3HJ, UK

³⁵ Instituto de Investigación en Astronomía y Ciencias Planetarias, Universidad de Atacama, Copayapu 485, Copiapó, Atacama, Chile

³⁶ Centre for Star and Planet Formation, Niels Bohr Institute, University of Copenhagen, Østervoldgade 5, DK-1350 Copenhagen, Denmark

³⁷ Universität Hamburg, Faculty of Mathematics, Informatics and Natural Sciences, Department of Earth Sciences, Meteorological Institute, Bundesstraße 55, D-20146 Hamburg, Germany

³⁸ Instituto de Astrofísica Pontificia Universidad Católica de Chile, Avenida Vicuña Mackenna 4860, Macul, Santiago, Chile

³⁹ Instituto de Astronomía y Ciencias Planetarias, Universidad de Atacama, Copayapu 485, Copiapó, Chile

⁴⁰ Zentrum für Astronomie der Universität Heidelberg, Astronomisches Rechen-Institut, Mönchhofstr. 12-14, D-69120 Heidelberg, Germany

⁴¹ Astronomy Research Center, Research Institute of Basic Sciences, Seoul National University, 1 Gwanak-ro, Gwanak-gu, Seoul 08826, Republic of Korea

⁴² Instituto de Astrofísica e Ciências do Espaço, Departamento de Física, Universidade de Coimbra, PT3040-004 Coimbra, Portugal

⁴³ Department of Physics, Sharif University of Technology, PO Box 11155-9161, Tehran, Iran

⁴⁴ Astrophysics Group, Keele University, Staffordshire ST5 5BG, UK

⁴⁵ Institute of Astronomy, Graduate School of Science, The University of Tokyo, 2-21-1 Osawa, Mitaka, Tokyo 181-0015, Japan

Received 2022 December 2; revised 2023 July 5; accepted 2023 July 18; published 2023 August 18

Abstract

We present an analysis of microlensing event OGLE-2019-BLG-0825. This event was identified as a planetary candidate by preliminary modeling. We find that significant residuals from the best-fit static binary-lens model exist and a xallarap effect can fit the residuals very well and significantly improves χ^2 values. On the other hand, by including the xallarap effect in our models, we find that binary-lens parameters such as mass ratio, q , and separation, s , cannot be constrained well. However, we also find that the parameters for the source system such as the orbital period and semimajor axis are consistent between all the models we analyzed. We therefore constrain the properties of the source system better than the properties of the lens system. The source system comprises a G-type main-sequence star orbited by a brown dwarf with a period of $P \sim 5$ days. This analysis is the first to demonstrate that the xallarap effect does affect binary-lens parameters in planetary events. It would not be common for the presence or absence of the xallarap effect to affect lens parameters in events with long orbital periods of the source system or events with transits to caustics, but in other cases, such as this event, the xallarap effect can affect binary-lens parameters.

Unified Astronomy Thesaurus concepts: [Gravitational microlensing \(672\)](#); [Brown dwarfs \(185\)](#); [Xallarap effect \(2139\)](#)

Supporting material: data behind figure

1. Introduction

The gravitational microlensing method is a method for detecting exoplanets that utilizes the phenomenon that light is deflected by gravity (Liebes 1964; Paczynski 1991) and is sensitive to planets beyond the snow line (Gould & Loeb 1992; Bennett & Rhie 1996). Giant planets are thought to form near and beyond the snow line (Ida & Lin 2004; Laughlin et al. 2004; Kennedy et al. 2006). In gravitational microlensing, when a lensing object crosses in front of a source star, the brightness of the source star changes with time owing to the gravitational effect of the lensing object. Furthermore, if this lensing object is accompanied by a planetary or binary-star companion, the gravity of this companion will cause a secondary magnification. The gravitational microlensing method does not use the light from the lensing object, but only the time-dependent variations arising from the gravitational effect of the lensing object or objects on the light from the source. Therefore, the gravitational microlensing method has the advantage over other planet detection methods of being able to detect planets around faint stars at large distances from Earth (Gaudi 2012). By comparing the occurrence rates of planets in the distant region detected by the gravitational microlensing method with the frequency of planets in the local

region, we can investigate the influence of the Galactic environment on planet formation.

The detection of distant planets and brown dwarfs allows us to consider the influence of the Galactic environment on planet and brown dwarf formation. It has been thought that different Galactic environments have different planetary occurrence rates (Gonzalez et al. 2001; Lineweaver et al. 2004; Spinelli et al. 2021). In fact, radial velocity surveys in the 25 pc region near the Sun reported that the occurrence rate of hot Jupiters is about $\sim 2\%$ (Hirsch et al. 2021), whereas Kepler transit surveys report that the occurrence rate of hot Jupiters around G- and K-type stars near Cygnus is about $\sim 0.5\%$ (Howard et al. 2012; Santerne et al. 2012, 2016; Fressin et al. 2013). Although Koshimoto et al. (2021) recently found that planetary frequencies do not depend significantly on the Galactocentric distance based on their sample of 28 planets, their result is still too uncertain to discuss environmental effects precisely.

In the analysis of gravitational microlensing events, it is sometimes difficult to distinguish perturbations given by the lens secondary to the light curve from those given by higher-order effects (Griest & Hu 1992; Rota et al. 2021). One of the higher-order effects, the parallax effect, is the effect of the acceleration of the Earth's orbital motion on the light curve. The xallarap effect is a higher-order effect on the light curve when the source is binary (Griest & Hu 1992; Han & Gould 1997; Paczynski 1997; Poindexter et al. 2005). Binary stars are common in the Universe, with binary systems of two or more stars accounting for about 30% of all stellar systems (Lada 2006; Badenes et al. 2018). When a source is accompanied by a companion star, the companion is not necessarily magnified, but the light curve is affected by the orbital motion of the source primary (Rota et al. 2021). Although the primary and companion stars of most binaries are too far apart

⁴⁶ The MOA Collaboration.

⁴⁷ The OGLE Collaboration.

⁴⁸ The KMTNet Collaboration.

⁴⁹ The MiNDSTEp Collaboration.



Table 1
Data Sets for OGLE-2019-BLG-0825

Observatory Sites	Telescope	Collaboration	Label	Filter	N_{use}	k^a	e_{min}^a
Mount John	MOA-II 1.8 m	MOA	MOA	MOA-Red	3949	1.330	0.009
				<i>V</i>	86	0.835	0
Las Campanas	Warsaw 1.3 m	OGLE	OGLE	<i>I</i>	1535	1.453	0.007
Siding Spring	KMTNet Australia 1.6 m	KMTNet	KMTA01 ^b	<i>I</i>	704	1.649	0
			KMTA41 ^c	<i>I</i>	719	1.613	0
Cerro Tololo Inter-American	KMTNet Chile 1.6 m		KMTC01 ^b	<i>I</i>	952	0.761	0.004
			KMTC41 ^c	<i>I</i>	954	1.436	0
South Africa Astronomical	KMTNet South Africa 1.6 m		KMTS01 ^b	<i>I</i>	881	1.490	0
			KMTS41 ^c	<i>I</i>	887	1.416	0
ESO's La Silla	Danish 1.54 m	MiNDSTEp	Danish	<i>I</i>	76	0.706	0

Notes.

^a Parameters for the error normalization.

^b Data observed in BLG01 in the overlapped area.

^c Data observed in BLG41 in the overlapped area.

to reliably detect a xallarap effect, a systematic survey of 22 long-term events in the bulge shows that 23% of them are indeed affected by xallarap (Poindexter et al. 2005). The effect of xallarap on the efficiency of detecting lensing planets has not been fully investigated but is known to exist (Zhu et al. 2017).

We present in this paper an analysis of OGLE-2019-BLG-0825 and report that the xallarap effect was detected and that the lensing system parameters changed before and after the xallarap effect was included. Section 2 describes the data for event OGLE-2019-BLG-0825. Section 3 describes our data reduction. Section 4 describes our modeling in detail. Section 5 derives the color and magnitude of the source and calculates the physical parameters of the source system from the color and magnitude of the source and the fitting parameters of the microlensing. Section 6 describes the estimation of the physical parameters of the lens system by Bayesian analysis. Finally, Section 7 discusses and summarizes the results of our analysis.

2. Observation

Microlensing event OGLE-2019-BLG-0825 was first discovered on 2019 June 3 (HJD' \sim 8638)⁵⁰ at J2000 equatorial coordinates (R.A., decl.) = (17^h52^m21^s.62, $-30^{\circ}48'13''$.2) corresponding to Galactic coordinates (l, b) = ($-0^{\circ}.849, -2^{\circ}.214$), by the Optical Gravitational Lensing Experiment (OGLE; Udalski 2003) collaboration. OGLE conducts a microlensing survey using the 1.3 m Warsaw Telescope with a CCD camera with a 1.4 deg² field of view (FOV) at Las Campanas Observatory in Chile and distributes alerts of the discovery of microlensing events by their OGLE-IV Early Warning System (Udalski et al. 1994, 2015; Udalski 2003). The event is located in the OGLE-IV field BLG534, which is observed on the Cousins *I* band with an hourly cadence (Mróz et al. 2019).

The Microlensing Observations in Astrophysics (MOA; Bond et al. 2001; Sumi et al. 2003) collaboration also independently discovered this event on 2019 June 23, and identified it as MOA-2019-BLG-273 using the MOA alert system (Bond et al. 2001). The MOA collaboration conducts a microlensing exoplanet survey toward the Galactic bulge using the 1.8 m MOA-II telescope with a CCD camera with a

2.2 deg² wide FOV, MOA-cam3 (Sako et al. 2008), at the University of Canterbury's Mount John Observatory in New Zealand. The MOA survey uses a custom wideband filter referred to as R_{MOA} , corresponding to the sum of the Cousins *R* and *I* bands. In addition, a Johnson *V*-band filter is used primarily for measuring the color of the source. The event is located in the MOA field gb4, which is observed with high cadence once every 15 minutes.

The Korea Microlensing Telescope Network (KMTNet; Kim et al. 2016) collaboration conducts a microlensing survey using three 1.6 m telescopes each with a CCD camera with a 4.0 deg² FOV. The telescopes are located at the Cerro Tololo Inter-American Observatory (CTIO) in Chile, the South African Astronomical Observatory (SAAO) in South Africa, and Siding Spring Observatory (SSO) in Australia. This event is located in an overlapping region with two KMTNet observed fields (KMTNet BLG01 and BLG41), which are observed with high cadence once every 15 minutes, and was discovered by the KMTNet EventFinder (Kim et al. 2018) as KMT-2019-BLG-1389 on 2019 June 28.

The Danish telescope of MiNDSTEp (Microlensing Network for the Detection of Small Terrestrial Exoplanets) made follow-up observations in the *I* band. MiNDSTEp uses the 1.54 m Danish Telescope at the European Southern Observatory at La Silla Observatory in Chile (Dominik et al. 2010). Data from the Spitzer space telescope (Yee et al. 2015) were also available, but these show no detectable signal and so are not used. A summary of all data sets used in the analysis of OGLE-2019-BLG-0825 is shown in Table 1.

The above data sets are used in our light-curve analysis. To reduce long-term systematics on the baseline, we used approximately two years of data over $8100 \leq \text{HJD}' \leq 8800$. Figure 1 shows the light curve of OGLE-2019-BLG-0825 and the standard binary-lens single-source model (hereafter, standard 2L1S), the binary-lens single-source with parallax effect model (hereafter, 2L1S + parallax), the single-lens single-source with xallarap effect model (hereafter 1L1S + xallarap), and the best-fit model (binary-lens single-source with xallarap effect model, hereafter 2L1S + xallarap), described in Section 4. As will be discussed in detail in Section 5, the xallarap model analysis assumes that the magnified flux of the second source is too weak to be detected, so it is denoted 1S.

⁵⁰ HJD' \equiv HJD - 2,450,000

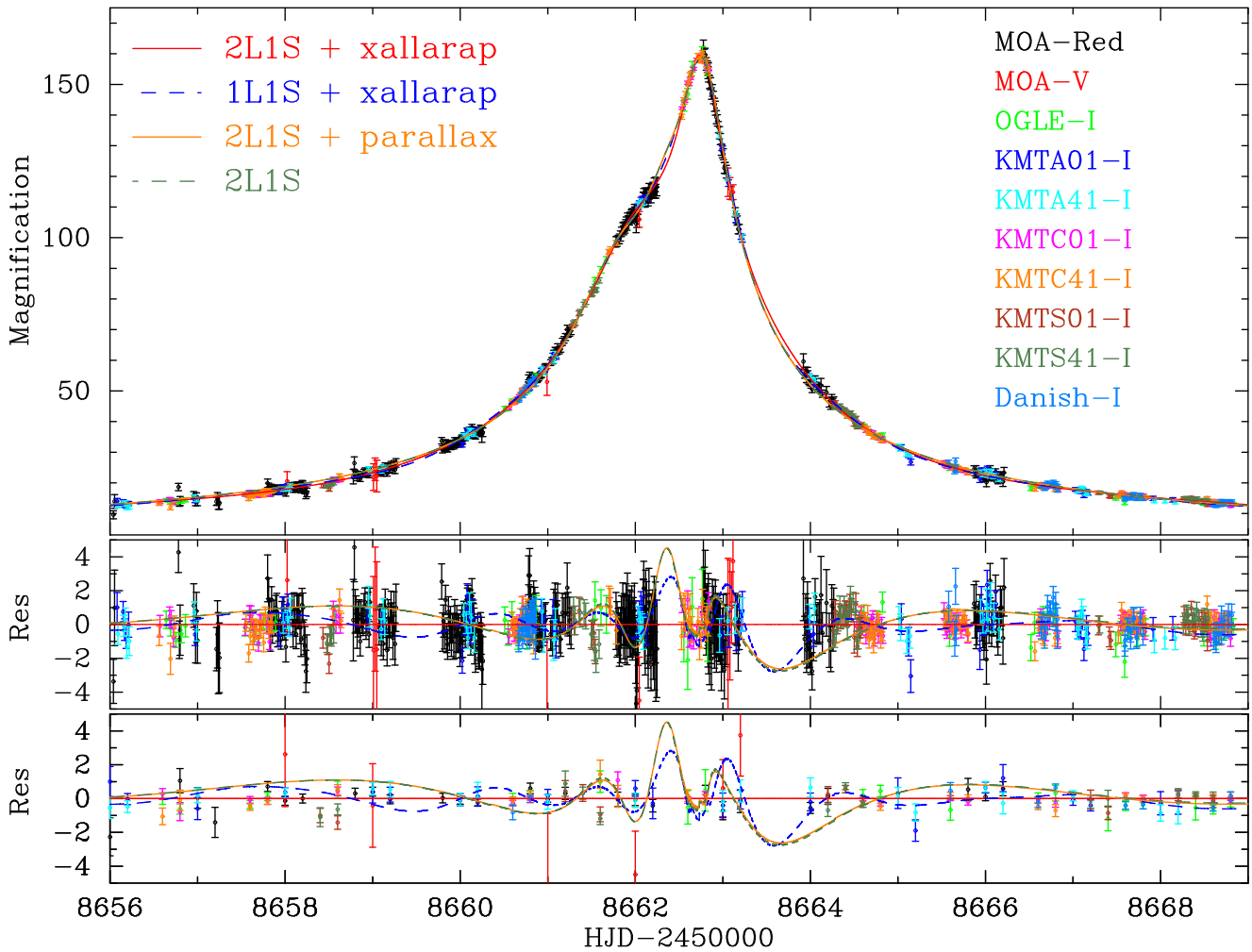


Figure 1. Top panel: light curve for OGLE-2019-BLG-0825. Error bars are renormalized according to Equation (1). The red solid, blue dashed, orange solid, and green dashed lines are the best 2L1S + xallarap model, the best 1L1S + xallarap model, the best 2L1S + parallax model and the best standard 2L1S model described in Section 4, respectively. Middle panel: residuals from the best 2L1S + xallarap model. Bottom panel: residuals from the best 2L1S + xallarap model binned by 0.2 days.

(The data used to create this figure are available.)

3. Data Reduction

The OGLE data were reduced with the OGLE difference image analysis (DIA, Wozniak 2000) photometry pipeline (Udalski 2003; Udalski et al. 2015), which uses the DIA technique (Tomany & Crotts 1996; Alard & Lupton 1998; Alard 2000). The MOA data were reduced with MOA’s implementation of the DIA photometry pipeline (Bond et al. 2001). The KMTNet data were reduced with their PySIS photometry pipeline (Albrow et al. 2009). The MiNDSTeP data were reduced using DanDIA (Bramich 2008; Bramich et al. 2013).

It is known that the nominal error bars calculated by the pipelines are incorrectly estimated in such crowded stellar fields. We follow a standard empirical error-bar normalization process (Yee et al. 2012) intended to estimate proper uncertainties for the lensing parameters in the light-curve modeling. This process, described below, hardly affects the best-fit parameters (Ranc et al. 2019). We renormalize the photometric error bars using the formula

$$\sigma'_i = k\sqrt{\sigma_i^2 + e_{\min}^2}, \quad (1)$$

in which σ'_i is the renormalized uncertainty in magnitude, while σ_i is an uncertainty of the i th original data point obtained from the photometric pipeline. The variables k and e_{\min} are renormalizing parameters. For preliminary modeling, we search for the best-fit lensing parameters using σ_i . We then construct a cumulative χ^2 distribution as a function of lensing magnification. The e_{\min} value is chosen so that the slope of the distribution is uniform (Yee et al. 2012). The k value is chosen so that $\chi^2/\text{d.o.f.} \simeq 1$ (d.o.f. is degrees of freedom). In Table 1, we list the calculated error-bar renormalization parameters.

4. Light-curve Modeling

The model flux for a microlensing event is given by the following equation:

$$f(t) = A(t, \mathbf{x})f_s + f_b, \quad (2)$$

where $A(t, \mathbf{x})$ is the source flux magnification, f_s is the flux of the source star, and f_b is the blend flux. In the 1L1S model, \mathbf{x} is described by four parameters (Paczynski 1986): the time of the

source closest to the center of mass, t_0 ; the Einstein radius crossing time, t_E ; the impact parameter, u_0 , and the source angular radius, ρ . Both u_0 and ρ are in units of the angular Einstein radius, θ_E .

For modeling the light curve, we used the Metropolis–Hastings Markov Chain Monte Carlo method. The finite source effect, an effect in which the source has a finite angular size, was calculated using the image-centered inverse-ray shooting method (Bennett & Rhie 1996; Bennett 2010) as implemented by Sumi et al. (2010). Note that f_s and f_b parameters are obtained from a linear fit using the method of Rhie et al. (1999). We adopt the following linear limb-darkening law for source brightness:

$$S_\lambda(\vartheta) = S_\lambda(0)[1 - u_\lambda(1 - \cos(\vartheta))], \quad (3)$$

where ϑ represents the angle between the line of sight and the normal to the surface of the source star. $S_\lambda(\vartheta)$ is a limb-darkening surface brightness of ϑ at wavelength λ . We estimated the effective temperature of the source star in Section 5 to be $T_{\text{eff}} = 5425 \pm 359$ K (González Hernández & Bonifacio 2009). In this analysis, we assume the source star’s metallicity $[M/H] = 0$, surface gravity $\log g = 4.5$, and microturbulent velocity $v = 1$ km s $^{-1}$. We use the limb-darkening coefficients $u_V = 0.685$, $u_R = 0.604$, and $u_I = 0.518$, which are taken from the ATLAS model with $T_{\text{eff}} = 5500$ K (Claret & Bloemen 2011). Since R_{MOA} covers both R - and I -band wavelengths, we adopted the average value $u_{R_{\text{MOA}}} = (u_R + u_I)/2 = 0.561$. In addition, as will be discussed in more detail in Section 7, we assume that the source of this event is a main-sequence star.

As the result of 1L1S model analysis, we found that $(t_0, t_E, u_0, \rho) = (8662.6, 47.6, 1.2 \times 10^{-2}, 4.8 \times 10^{-3})$ is the best solution. This best 1L1S model is $\Delta\chi^2 = 21,400$ worse than the best standard 2L1S model.

4.1. Standard Binary Lens

In the standard 2L1S model, three additional parameters are required: the mass ratio of a lens companion relative to the host, q ; the projected separation normalized by Einstein radius between binary components, s ; and the angle between the binary-lens axis and the direction of the source trajectory, α .

Because the χ^2 surface of the microlensing parameter has a very complicated shape, 34,440 values of (q, s, α) , which have a particularly large impact on the shape of the light curve, were initially fixed in the fitting process. Here we uniformly take 21 values in the range $-5 \leq \log q \leq 0$, 41 values in the range $-1.25 \leq \log s \leq 1.25$, and 40 values in the range $0 \leq \alpha \leq 2\pi$. For the top 1000 combinations that gave good fits, we performed the fitting again with q, s , and α free. This process minimizes the chance that we miss local solutions even in a large and complex microlensing parameter space. The left panel of Figure 2 shows the results of the grid search analysis for the standard 2L1S model.

As a result of the analysis, the best-fit standard 2L1S model is $(q, s) = (3.3 \times 10^{-3}, 0.57)$ (close1). Hereafter, we call solutions with $s < 1$ and $s > 1$ “close” and “wide,” respectively. We call the best standard 2L1S close1. We also found local minima at $(q, s) = (3.4 \times 10^{-3}, 1.75)$ (wide1) with $\Delta\chi^2 \sim 0.4$, $(q, s) = (2.1 \times 10^{-2}, 0.28)$ (close2) with $\Delta\chi^2 \sim 20.4$, and $(q, s) = (2.1 \times 10^{-2}, 3.78)$ (wide2) with $\Delta\chi^2 \sim 23.3$. Detailed parameters of the standard binary models are shown in Table 2.

However, we observed systematic residuals around the peak of $8657 < \text{HJD}' < 8667$ in these models, as depicted by the green dashed line in Figure 1. In Figure 1, we plot only close1, the best for the standard 2L1S, but the other three models also have similar residuals. We therefore proceed to model the light curve with higher-order effects.

4.2. Parallax

It is known that the acceleration of Earth’s orbital motion affects the light curve of microlensing events (Gould 1992, 2004; Smith et al. 2003; Dong et al. 2009). This parallax effect can be described by the microlensing parallax vector $\boldsymbol{\pi}_E = (\pi_{E,N}, \pi_{E,E})$ where $\pi_{E,N}$ and $\pi_{E,E}$ represent respectively the north and east components of $\boldsymbol{\pi}_E$ projected onto the sky plane in equatorial coordinates. The direction of $\boldsymbol{\pi}_E$ is defined to coincide with the direction of the geocentric lens–source relative proper motion projected onto the sky plane at the reference time t_{fix} , and the amplitude of $\boldsymbol{\pi}_E$ is $\pi_E = au/\tilde{r}_E$ (\tilde{r}_E is the Einstein radius projected inversely to the observation plane; Gould 2000).

As a result of modeling by adding the two parameters $\pi_{E,N}$ and $\pi_{E,E}$, we found two degenerate models with $(q, s) = (3.5 \times 10^{-3}, 0.57)$ and $(q, s) = (3.4 \times 10^{-3}, 1.74)$, which are better than the standard 2L1S model by $\Delta\chi^2 = 68.3$. However, the cumulative $\Delta\chi^2$ improvement for parallax model relative to standard 2L1S model is not consistent between the data sets. Furthermore, we still found systematic residuals around the peak of $8657 < \text{HJD}' < 8667$ in these models, as seen in the standard 2L1S model shown by the orange solid line in Figure 1.

4.3. Xallarap

We next consider the possibility that the short-term residuals in $8657 < \text{HJD}' < 8667$ are caused by a short-period binary source system, i.e., they arise owing to the xallarap effect.

The xallarap effect can be described by the following seven parameters: the direction toward the solar system relative to the orbital plane of the source system, R.A. $_\xi$ and decl. $_\xi$; the source orbital period, P_ξ ; the source orbital eccentricity, e_ξ ; the perihelion, T_{peri} ; and the xallarap vector, $\boldsymbol{\xi}_E = (\xi_{E,N}, \xi_{E,E})$. Note that this effect does not include the magnifying effect of the source companion star; only the source host contributes to the magnification. We denote this model of the microlensing event as the 2L1S + xallarap model rather than as the 2L2S model to distinguish it from a model including secondary source magnification. As discussed in detail in Section 5, the flux ratio of the source companion to the host star in the I band in the best 2L1S + xallarap model is $\sim 10^{-7}$. Therefore, we assume that the brightening of the source companion star is negligible.

We first fit using 78,960 values of xallarap parameters (R.A. $_\xi$, decl. $_\xi$, P_ξ) with the four best standard 2L1S models (close1, wide1, close2, and wide2) as initial values. We used 20 evenly spaced values for $0^\circ \leq \text{R.A.}_\xi < 360^\circ$, 21 values for $-90^\circ \leq \text{decl.}_\xi < 90^\circ$, and 19 and 99 values for $1 \leq P_\xi$ [days] ≤ 19 and $20 \leq P_\xi$ [days] ≤ 1000 , respectively. After that, we fit again with (R.A. $_\xi$, decl. $_\xi$, P_ξ) as free parameters. As a result, we found the best solutions with $P_\xi \sim 5$ days independently from the initial values of close1, wide1, close2, and wide2. We also found that the final q and s values are quite different from their initial values, and did not converge. Therefore, we next set $P_\xi \sim 5$ days as the initial value, R.A. $_\xi$ and decl. $_\xi$ to random values, and performed model fitting with 34,440

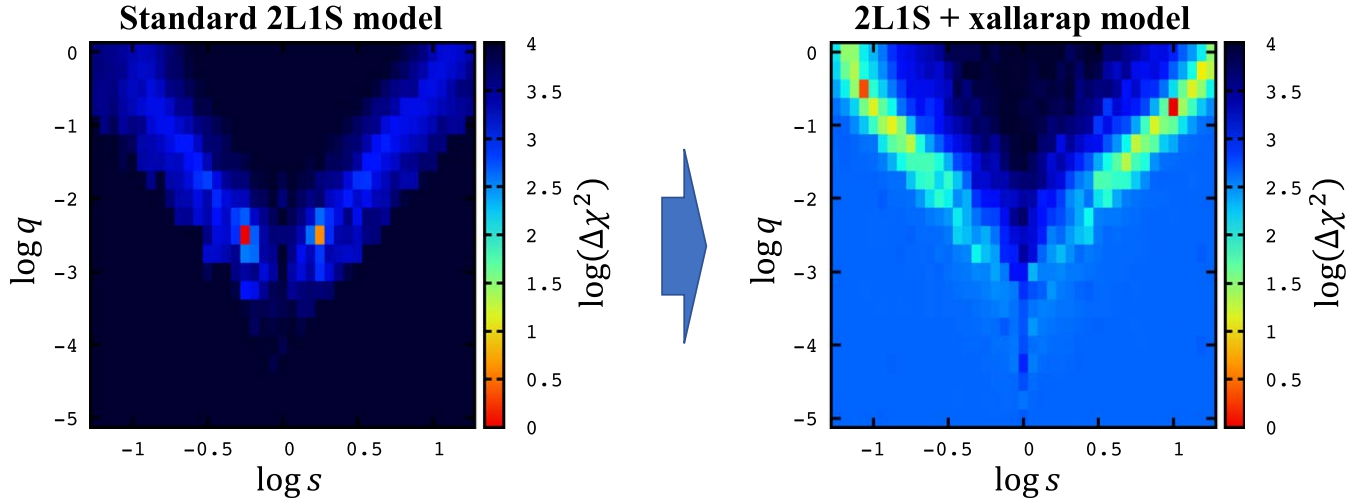


Figure 2. Map of $\Delta\chi^2$ in each s - q grid from the (q, s, α) grid search for the standard 2L1S model (left) and for the 2L1S + xallarap model (right). The best-fit α is chosen for each grid location. In the map of the standard 2L1S model, we found the best solution at $q \sim 10^{-3}$. However, for the 2L1S + xallarap map, best solutions at two other local minima appear at $q > 0.1$.

Table 2
Parameters of the Standard 2L1S Models

Model	close1	close2	wide1	wide2
t_0 (HJD - 2,458,660)	2.474 ± 0.001	2.483 ± 0.001	2.473 ± 0.001	2.489 ± 0.001
t_E (days)	74.7 ± 2.0	75.7 ± 2.0	72.8 ± 1.8	77.3 ± 2.0
u_0 (10^{-3})	7.30 ± 0.21	7.11 ± 0.19	7.53 ± 0.19	6.91 ± 0.19
q (10^{-3})	3.30 ± 0.11	20.71 ± 9.84	3.39 ± 0.10	21.33 ± 1.15
s	0.569 ± 0.004	0.207 ± 0.038	1.747 ± 0.011	3.776 ± 0.063
α (rad)	5.034 ± 0.002	2.766 ± 0.002	5.036 ± 0.003	2.767 ± 0.002
ρ (10^{-3})	2.95 ± 0.09	0.48 ± 0.28	3.02 ± 0.09	0.47 ± 0.14
χ^2	11,744.7	11,765.1	11,745.1	11,768.0
$\Delta\chi^2$...	20.4	0.4	23.3

values of (q, s, α) using the same procedure as the standard 2L1S modeling described in Section 4.1. Short-period binary stars orbiting in $P_\xi \sim 5$ days are affected by orbital circularization due to tidal friction (Fabrycky & Tremaine 2007). The tidal circularization time is discussed in Section 7, but it is reasonable to assume that at the age of the stars in the Galactic bulge (Sit & Ness 2020), the orbit is fully circularized. Therefore, we fixed the eccentricity at $e_\xi = 0$. When $e_\xi = 0$, T_{peri} can be eliminated as a fitting parameter. The results are shown in the right panel of Figure 2.

The figure shows that there are degenerate solutions for various combinations of (q, s) values in the range of $\Delta\chi^2 \lesssim 20$. Table 3 shows the best-fit model parameters for the wide and close solutions. The reason for the slight difference in $\Delta\chi^2$ between Figure 2 and Table 3 is that the models in Table 3 were fitted with q, s , and α set free. We label the best models of the mass-ratio range in the 2L1S + xallarap close model, respectively: the best with $q \leq 0.1$ is XLclose1, the best with $0.1 < q \leq 1$ is XLclose2. Similarly, in the wide model of 2L1S + xallarap, we label the best with $q \leq 0.1$ as XLwide1, the best with $0.1 < q \leq 1$ as XLwide2. Figure 1 shows the best 2L1S + xallarap model (i.e., XLclose2). The xallarap models fit the light curves better than the standard 2L1S models.

Figure 3 shows the cumulative $\Delta\chi^2$ of the best 2L1S + xallarap model relative to the best standard 2L1S model. One can see that the 2L1S + xallarap model improves χ^2 around the

peak of $8657 < \text{HJD}' < 8667$. The 2L1S + xallarap model improved χ^2 by 903.7 from the standard 2L1S model and by 835.5 from the 2L1S + parallax model. Figure 4 shows the geometry of the primary lens, the source trajectory, and caustics on the magnification map for the best 2L1S + xallarap model. The short orbital period of the source star with $P_\xi \sim 5$ days makes the source's trajectory a wavy line.

We applied the same procedure for 1L1S and found the best 1L1S + xallarap model has $\Delta\chi^2 = 470.6$ worse than the best 2L1S + xallarap model. However, asymmetric maps similar to Figure 4 can be created by binary lenses of various parameters, which led to the emergence of various degenerate 2L1S + xallarap models. We label the best 1L1S + xallarap model as 1LXL. Even the 1L1S + xallarap + parallax model was $\Delta\chi^2 = 444.8$ worse than the best 2L1S + xallarap model. We label the best 1L1S + xallarap + parallax model as 1LXLPL. The parameters of each of the best models are listed in Table 4.

We considered other higher-order effects and combinations of them such as 2L1S + xallarap + parallax, 2L1S + xallarap + parallax + lens orbital motion, and 1L2S, but could not detect them significantly. For comparison with the 2L1S + xallarap model, we also fitted the 2L1S model with a variable source. In this case, the amplitude of the variation, γ , the period of the variation, T_v , and the initial phase, β , are additional parameters. We fixed the other parameters to those of the best standard 2L1S model (i.e., close1). However, the χ^2 improvement from

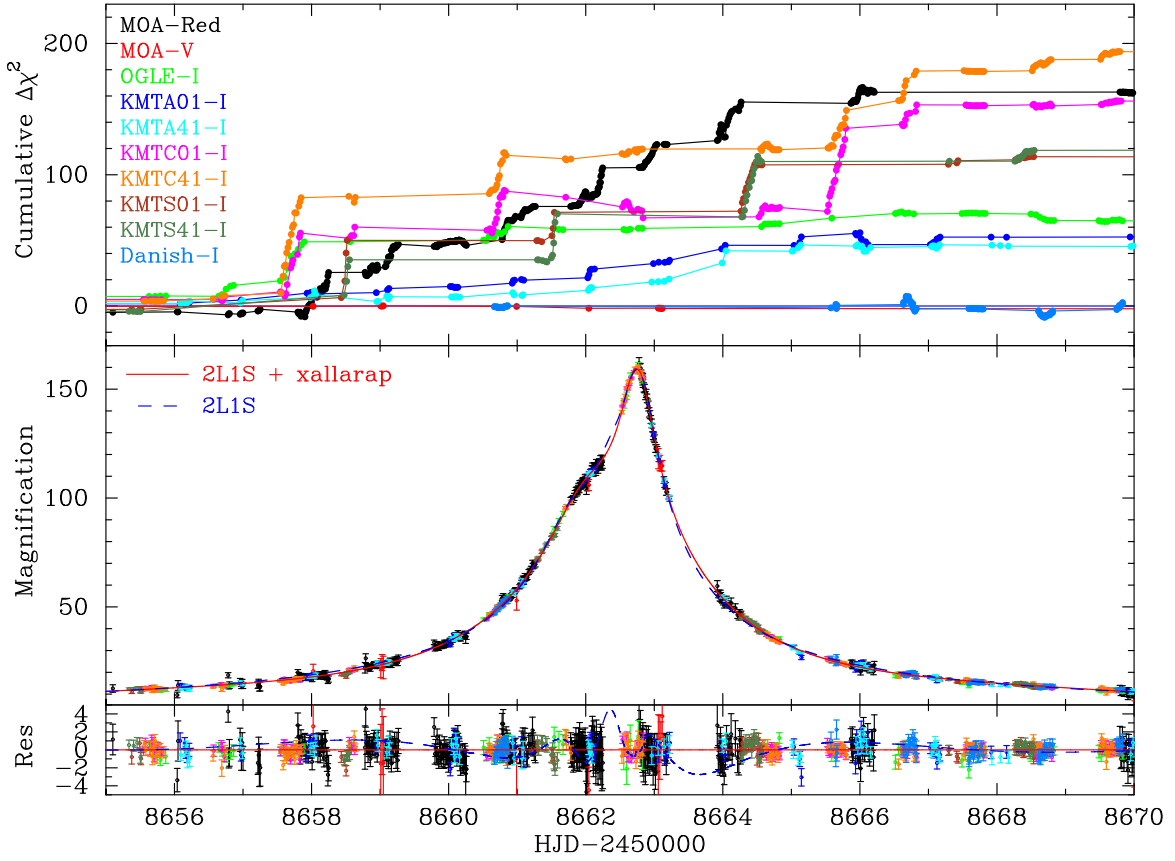


Figure 3. Top panel: cumulative $\Delta\chi^2$ for the xallarap model compared to the standard binary-lens model. Each color corresponds to each instrument listed on the left side of the image. Middle panel: the light curve of the best 2L1S + xallarap model (solid red line) and the light curve of the standard 2L1S best model (blue dashed line). Bottom panel: residuals of the light curves from the 2L1S + xallarap model.

Table 3
Parameters of the 2L1S + Xallarap Models, 1L1S + Xallarap Model, and 1L1S + Xallarap + Parallax Model

Model	XLclose1	XLclose2	XLwide1	XLwide2	1LXL	1LXLPL
Range of q	$q \leq 0.1$	$0.1 < q \leq 1$	$q \leq 0.1$	$0.1 < q \leq 1$
t_0 (HJD - 2,458,660)	2.576 ± 0.005	2.573 ± 0.007	2.572 ± 0.004	2.575 ± 0.006	2.744 ± 0.001	2.744 ± 0.001
t_E (days)	97.7 ± 2.6	93.8 ± 3.1	100.7 ± 3.4	133.3 ± 11.5	67.2 ± 2.0	73.5 ± 1.5
u_0 (10^{-3})	-7.16 ± 0.22	-6.98 ± 0.21	7.06 ± 0.21	4.91 ± 0.35	6.93 ± 0.20	6.31 ± 0.14
q	0.09 ± 0.01	0.44 ± 0.11	0.10 ± 0.01	0.94 ± 0.37
s	0.141 ± 0.004	0.085 ± 0.004	7.403 ± 0.438	$18,040 \pm 1.263$
α (rad)	0.429 ± 0.008	1.937 ± 0.010	5.846 ± 0.008	4.350 ± 0.009
ρ (10^{-3})	2.56 ± 0.13	2.15 ± 0.12	2.41 ± 0.11	1.44 ± 0.16	7.04 ± 0.20	6.41 ± 0.14
R.A. $_{\xi}$ (deg)	81.6 ± 11.7	153.2 ± 10.5	75.9 ± 14.5	155.4 ± 8.5	31.3 ± 0.5	32.1 ± 0.5
decl. $_{\xi}$ (deg)	54.5 ± 10.5	36.9 ± 16.4	-79.4 ± 12.8	-40.7 ± 14.1	9.9 ± 0.2	9.9 ± 0.3
P_{ξ} (days)	5.42 ± 0.04	5.53 ± 0.05	5.43 ± 0.04	5.54 ± 0.05	2.91 ± 0.02	2.9 ± 0.02
$\xi_{E,N}$ (10^{-3})	1.82 ± 0.15	-0.36 ± 0.36	-1.65 ± 0.11	0.34 ± 0.20	-3.59 ± 0.11	-3.23 ± 0.08
$\xi_{E,E}$ (10^{-3})	0.69 ± 0.34	1.53 ± 0.12	0.42 ± 0.41	1.07 ± 0.10	2.86 ± 0.09	2.58 ± 0.07
$\pi_{E,N}$	0.09 ± 0.05
$\pi_{E,E}$	0.26 ± 0.14
χ^2	10,856.4	10,840.9	10,861.2	10,842.7	11,311.5	11,285.7
$\Delta\chi^2$	15.5	-	20.3	1.8	470.6	444.8

the best standard 2L1S model was only 139.1, $\Delta\chi^2 = 764.6$ worse than the best 2L1S + xallarap model. To confirm, we performed 2L1S + xallarap fitting analysis with $\xi_{E,N}$, $\xi_{E,E}$, R.A. $_{\xi}$, decl. $_{\xi}$, and P_{ξ} set free and the other parameters fixed to the best standard 2L1S model. As a result, χ^2 was improved by 594.5 over the best standard 2L1S model. This is only $\Delta\chi^2 = 309.3$ worse than the best 2L1S + xallarap model. That

is, for two models (2L1S + xallarap and 2L1S + variable source) with the same fixed lens parameters, the 2L1S + xallarap model has 455.3 better χ^2 than the 2L1S + variable source model. Finally, we conclude that the best model in this analysis is XLclose2. In addition, the xallarap signal is consistent, and considering additional higher-order effects on 2L1S + xallarap has little influence on our conclusions.

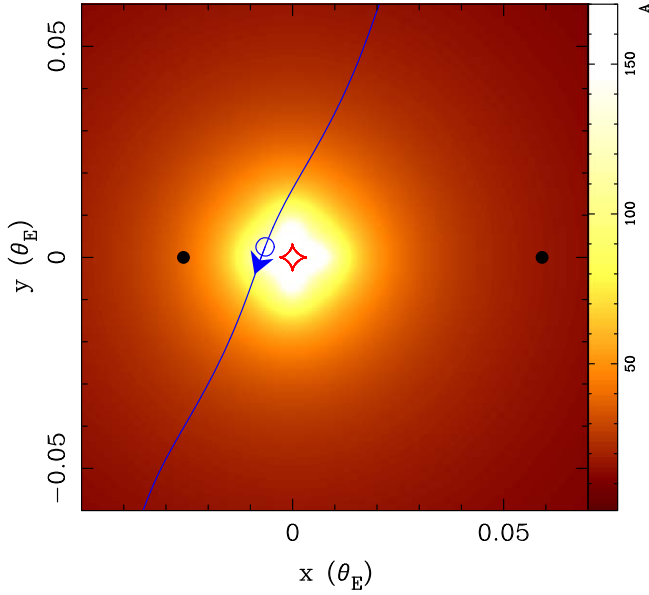


Figure 4. The geometry of the primary lens, the source trajectory, and caustics on the magnification map for the best 2L1S + xallarap model. The black filled circle on the left indicates the primary lens. The black filled circle on the right indicates the lens companion. The blue line with arrow represents the source trajectory. The blue circle represents the source size and position at t_0 . The red closed curve represents the caustic. The colored contours represent the magnification map.

Table 4
Comparisons between Each Microlensing Model

Model	N_{param}	χ^2	$\Delta\chi^2$
1L1S	4	33,144.7	22,303.8
1L1S + xallarap	9 ^a	11,311.5	470.6
1L1S + xallarap + parallax	11 ^a	11,285.7	444.8
Standard 2L1S	7	11,744.7	903.7
2L1S + parallax	9	11,676.5	835.5
2L1S + xallarap	12 ^a	10,840.9	...

Note.

^a The source orbital eccentricity is fixed at $e_\xi = 0$. When $e_\xi = 0$, T_{peri} can be eliminated because it is a parameter that cannot take a specific value.

5. Source System Properties

We estimated the angular source radius, θ_* , from the color and magnitude of the source. The best-fit instrumental source magnitudes of R_{MOA} and V_{MOA} are calibrated to the Cousins I -band and Johnson V -band magnitude scales by cross-referencing to the stars in the OGLE-III photometry map (Szymański et al. 2011) within $0''.7$ of the event.

For reliability, we restricted stars to $16 \leq V_{\text{OGLE-III}} [\text{mag}] \leq 19$, and performed 5σ clipping in the linear regressions of V_{MOA} versus $V_{\text{OGLE-III}}$, $(I_{\text{OGLE-III}} - R_{\text{MOA}})$ versus $(V - R)_{\text{MOA}}$, and $(V - I)_{\text{OGLE-III}}$ versus $(V - R)_{\text{MOA}}$. From the final 73 remaining objects, the following conversion equations from R_{MOA} and $(V - R)_{\text{MOA}}$ to $I_{\text{OGLE-III}}$ and $(V - I)_{\text{OGLE-III}}$ were obtained by linear regression:

$$\begin{aligned} I_{\text{OGLE-III}} &= R_{\text{MOA}} - (0.24 \pm 0.01) \\ &\times (V - R)_{\text{MOA}} + (27.22 \pm 0.01), \end{aligned} \quad (4)$$

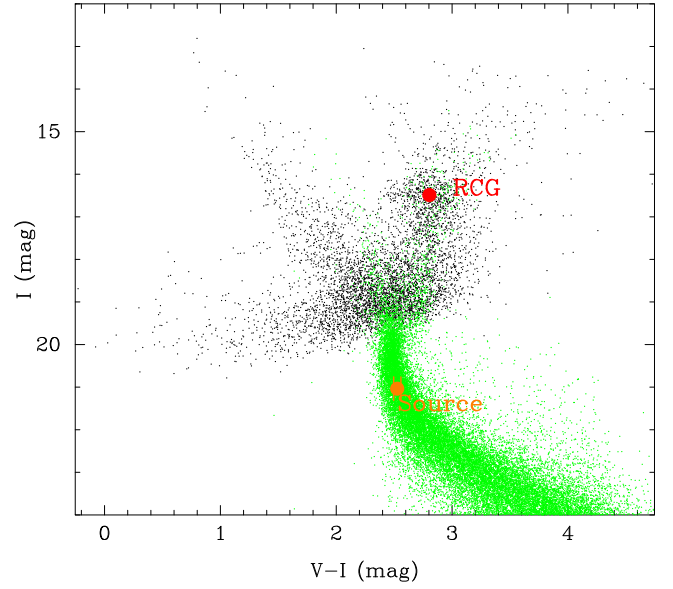


Figure 5. Color–magnitude diagram (black dots) of the OGLE-III stars within $2'$ around OGLE-2019-BLG-0825. The green dots are stars in Baade’s window based on Hubble Space Telescope observations (Holtzman et al. 1998), color- and magnitude-matched at the RCG position. The orange circles represent the positions of the source, and the red dots represent the positions of the RCG centroid within $2'$ around OGLE-2019-BLG-0825.

$$\begin{aligned} (V - I)_{\text{OGLE-III}} &= (1.20 \pm 0.01) \\ &\times (V - R)_{\text{MOA}} + (0.94 \pm 0.02). \end{aligned} \quad (5)$$

As a result, the color and magnitude with the extinction of the source star for the best-fit 2L1S + xallarap model were $(V - I, I)_{\text{S}} = (2.527 \pm 0.031, 21.035 \pm 0.015)$. The intrinsic color and magnitude of red clump giant (RCG) stars are $(V - I, I)_{\text{RCG,0}} = (1.060 \pm 0.060, 14.443 \pm 0.040)$ (Bensby et al. 2013; Nataf et al. 2013). From the color–magnitude diagram of the stars within $2'$ of the source star (Figure 5), the RCG centroid is estimated as $(V - I, I)_{\text{RCG}} = (2.804 \pm 0.009, 16.488 \pm 0.022)$. Then we calculated $(E(V - I), A(I)) = (1.744 \pm 0.061, 2.045 \pm 0.046)$. Finally, we have the intrinsic color and magnitude of the source star $(V - I, I)_{\text{S,0}} = (0.783 \pm 0.068, 18.990 \pm 0.048)$ for the best 2L1S + xallarap model. Also, Figure 5 shows that the source is a main-sequence star and unlikely to be a variable star. Table 5 shows that the values for $(V - I, I)_{\text{S,0}}$ for the other models are almost the same.

We estimated the angular source radius of $\theta_* = 0.538 \pm 0.039 \mu\text{as}$ from the relation

$$\log(2\theta_*) = 0.50 + 0.42(V - I)_0 - 0.2I_0, \quad (6)$$

where the accuracy of the relational equation is better than 2% (Fukui et al. 2015). This relation is based on Boyajian et al. (2014), but derived by limiting to FGK stars with $3900 < T_{\text{eff}} [\text{K}] < 7000$ (T. S. Boyajian 2014, private communication). Then, we calculated the lens’s Einstein radius of $\theta_{\text{E}} = \rho\theta_* = 0.25 \pm 0.02 \text{ mas}$ and the lens–source relative proper motion of $\mu_{\text{rel}} = \theta_{\text{E}}/t_{\text{E}} = 0.97 \pm 0.10 \text{ mas yr}^{-1}$.

The amplitude of the xallarap vector, ξ_{E} , is described as follows:

$$\xi_{\text{E}} \equiv \left(\frac{\theta_{\text{E}} D_{\text{S}}}{1 \text{ au}} \right)^{-1} \left(\frac{P_{\xi}}{1 \text{ yr}} \right)^{2/3} \left(\frac{M_{\text{S,C}}}{M_{\odot}} \right) \left(\frac{M_{\text{S,H}} + M_{\text{S,C}}}{M_{\odot}} \right)^{-2/3}, \quad (7)$$

Table 5
Source System Properties of the 2LIS + Xallarap Models

Model Range of q	XLclose1 $q \leq 0.1$	XLclose2 $0.1 < q \leq 1$	XLwide1 $q \leq 0.1$	XLwide2 $0.1 < q \leq 1$
V_S (mag)	23.58 ± 0.03	23.56 ± 0.03	23.55 ± 0.03	23.56 ± 0.03
I_S (mag)	21.06 ± 0.01	21.04 ± 0.01	21.02 ± 0.01	21.06 ± 0.01
H_S (mag)	18.54 ± 0.30	18.52 ± 0.484	18.51 ± 0.48	18.54 ± 0.48
K_S (mag)	18.31 ± 0.48	18.29 ± 0.48	18.28 ± 0.48	18.31 ± 0.48
$(V - I)_S$ (mag)	2.52 ± 0.03	2.53 ± 0.03	2.52 ± 0.03	2.527 ± 0.03
$I_{S,0}$ (mag)	19.01 ± 0.05	18.99 ± 0.05	19.00 ± 0.05	19.01 ± 0.05
$(V - I)_{S,0}$ (mag)	0.78 ± 0.07	0.78 ± 0.07	0.78 ± 0.07	0.78 ± 0.07
M_I (mag)	4.50 ± 0.38	4.48 ± 0.38	4.46 ± 0.38	4.50 ± 0.38
θ_E (mas)	0.53 ± 0.04	0.25 ± 0.02	0.22 ± 0.02	0.37 ± 0.05
μ_{rel} (mas yr $^{-1}$)	0.78 ± 0.07	0.97 ± 0.10	0.81 ± 0.07	1.01 ± 0.16
$M_{S,H}$ (M_\odot)	0.864 ± 0.045	0.867 ± 0.045	0.868 ± 0.045	0.864 ± 0.045
$M_{S,C}$ (M_\odot)	0.050 ± 0.005	0.048 ± 0.004	0.047 ± 0.004	0.051 ± 0.006
a_S (10^{-2} au)	5.86 ± 0.04	5.94 ± 0.05	5.87 ± 0.03	5.95 ± 0.05
$L_{S,C}/L_{S,H}$ (10^{-7})	1.15 ± 0.34	1.02 ± 0.26	0.95 ± 0.23	1.21 ± 0.47
χ^2	10,856.4	10,840.9	10,861.2	10,842.7
$\Delta\chi^2$	15.5	...	20.3	1.8

where $M_{S,H}$ and $M_{S,C}$ are the masses of host and companion of the source system, respectively. $M_{S,H}$ is estimated by using isochrones (PARSEC; Bressan et al. 2012) and the absolute magnitude of the host source star $M(I_S) = I_{S,0} + 5 \log_{10} D_S [\text{pc}] + 5 = 4.48 \pm 0.38$ mag assuming $D_S = 8.0 \pm 1.4$ kpc. Then, $M_{S,C}$ can be solved from Equation (7). Also, using Kepler's third law,

$$\left(\frac{a_S}{1 \text{ au}}\right)^3 \left(\frac{P_\xi}{1 \text{ yr}}\right)^{-2} = \frac{M_{S,H} + M_{S,C}}{M_\odot}, \quad (8)$$

we can solve a_S , which is the semimajor axis of the source system. The apparent H - and K -band magnitudes of the source with extinction H_S and K_S are also estimated using PARSEC isochrones and the wavelength dependence of the extinction law in the direction of Galactic center, $A_V : A_H : A_K = 1 : 0.108 : 0.062$ (Nishiyama et al. 2008). In addition, we calculated $L_{S,C}/L_{S,H}$, the luminosity ratio in the I band of the source companion $L_{S,C}$ to the source host $L_{S,H}$. For this we used the mass–luminosity empirical relation of Bennett et al. (2015), which combines Henry & McCarthy (1993) and Delfosse et al. (2000), and the isochrone model of Baraffe et al. (2003). We used the Henry & McCarthy (1993) relation for $M > 0.66 M_\odot$ and the Delfosse et al. (2000) relation for $0.12 M_\odot < M < 0.54 M_\odot$. For low-mass stars ($M < 0.10 M_\odot$) we used the isochrone model of Baraffe et al. (2003) for substellar objects at an age of 10 Gyr. At the boundary of these mass ranges, we interpolated linearly between the two relations. Table 5 shows our calculated properties of the source system for the 2LIS + xallarap models in Table 3. The source host in the best 2LIS + xallarap model is a G-type main-sequence star and the source companion is a brown dwarf with a semimajor axis of $a_S = 0.0594 \pm 0.0005$ au. The luminosity ratio in the I band of the source companion $L_{S,C}$ is small, $L_{S,C}/L_{S,H} = (1.0 \pm 0.3) \times 10^{-7}$, and does not conflict with our assumption that the magnified flux of the second source is too weak to be detected.

6. Lens System Properties by Bayesian Analysis

The distance from the Earth to the lensing system, D_L , and the total mass of the host and companion in the lensing system, M_L , can be described by the following equations (Gaudi 2012):

$$D_L = \frac{\text{au}}{\pi_E \theta_E + \pi_S}, \quad (9)$$

$$M_L = \frac{\theta_E}{\kappa \pi_E}, \quad (10)$$

where $\kappa = 4G/(c^2 \text{ au}) \sim 8.144 \text{ mas } M_\odot^{-1}$ and π_S is the parallax of the source star written as $\pi_S = \text{au}/D_S$.

Since the parallax effect was not detected in this event, we conducted a Bayesian analysis (Beaulieu et al. 2006; Gould et al. 2006; Bennett et al. 2008) to estimate the parameters of the lens system for the 2LIS + xallarap models. For the prior probability distributions, we used the mass density and velocity distributions of the Galaxy model from Han & Gould (1995), and we used the mass function from Sumi et al. (2011). Since the prior distribution only considers a single star, we scaled the event timescale and the Einstein radius to match those of the lens host so that the physical parameters of the lens host and companion can be properly estimated. The event timescale of the lens host $t_{E,H}$ and the Einstein radius of the lens host $\theta_{E,H}$ are expressed using the mass ratio q as follows:

$$t_{E,H} = \frac{t_E}{\sqrt{1+q}}, \quad (11)$$

$$\theta_{E,H} = \frac{\theta_E}{\sqrt{1+q}}. \quad (12)$$

We also estimated the apparent magnitudes of the lens system in the V , I , K , and H bands with extinction. The magnitudes were obtained using the mass–luminosity relation for main-sequence stars (Henry & McCarthy 1993; Kroupa & Tout 1997) and the isochrone model for 5 Gyr old substellar objects (Baraffe et al. 2003). The blending flux f_b from the light-curve modeling was used as the upper limit of the lens brightness. Following Bennett et al. (2015), we estimated the

Table 6
Lens System Properties of the 2L1S + Xallarap Models

Model	XLclose1	XLclose2	XLwide1	XLwide2
Range of q	$q \leq 0.1$	$0.1 < q \leq 1$	$q \leq 0.1$	$0.1 < q \leq 1$
D_L (kpc)	$7.27^{+1.10}_{-1.17}$	$7.24^{+1.09}_{-1.17}$	$7.24^{+1.09}_{-1.18}$	$7.12^{+1.05}_{-1.214}$
$M_{L,H}$ (M_\odot)	$0.23^{+0.28}_{-0.12}$	$0.25^{+0.29}_{-0.13}$	$0.26^{+0.29}_{-0.13}$	$0.37^{+0.32}_{-0.19}$
$M_{L,C}$ (M_\odot)	$0.02^{+0.03}_{-0.01}$	$0.11^{+0.13}_{-0.06}$	$0.03^{+0.03}_{-0.01}$	$0.35^{+0.30}_{-0.18}$
$a_{L,\perp}$ (au)	$0.20^{+0.04}_{-0.04}$	$0.13^{+0.02}_{-0.02}$	$11.55^{+2.03}_{-2.09}$	$34.74^{+7.51}_{-7.69}$
$a_{L,\text{exp}}$ (au)	$0.25^{+0.13}_{-0.06}$	$0.16^{+0.08}_{-0.04}$	$13.91^{+7.39}_{-3.15}$	$42.10^{+21.78}_{-10.92}$
$V_{L,H}$ (mag)	$30.61^{+2.56}_{-2.54}$	$30.34^{+2.42}_{-2.66}$	$30.25^{+2.31}_{-2.71}$	$29.17^{+1.83}_{-3.38}$
$I_{L,H}$ (mag)	$26.09^{+1.66}_{-1.75}$	$25.90^{+1.57}_{-1.83}$	$25.84^{+1.51}_{-1.86}$	$25.05^{+1.22}_{-2.35}$
$H_{L,H}$ (mag)	$22.53^{+1.27}_{-1.73}$	$22.35^{+1.26}_{-1.80}$	$22.30^{+1.23}_{-1.82}$	$21.53^{+1.17}_{-2.02}$
$K_{L,H}$ (mag)	$22.11^{+1.21}_{-1.70}$	$21.93^{+1.20}_{-1.75}$	$21.87^{+1.18}_{-1.77}$	$21.12^{+1.14}_{-1.94}$
$V_{L,C}$ (mag)	$41.53^{+0.98}_{-1.76}$	$33.68^{+6.20}_{-2.97}$	$41.42^{+1.03}_{-2.13}$	$29.35^{+1.88}_{-3.13}$
$I_{L,C}$ (mag)	$35.24^{+1.75}_{-3.05}$	$28.13^{+3.32}_{-1.94}$	$34.85^{+1.88}_{-3.13}$	$25.18^{+1.25}_{-2.16}$
$H_{L,C}$ (mag)	$33.74^{+3.00}_{-3.99}$	$24.12^{+5.98}_{-1.50}$	$33.42^{+3.12}_{-4.24}$	$21.66^{+1.16}_{-1.92}$
$\bar{K}_{L,C}$ (mag)	$30.45^{+1.47}_{-2.24}$	$23.63^{+3.68}_{-1.44}$	$30.00^{+1.54}_{-2.24}$	$21.25^{+1.14}_{-1.85}$
$V_{L,\text{total}}$ (mag)	$30.60^{+2.55}_{-2.54}$	$30.29^{+2.46}_{-2.68}$	$30.25^{+2.31}_{-2.71}$	$28.50^{+1.85}_{-3.27}$
$I_{L,\text{total}}$ (mag)	$26.08^{+1.65}_{-1.75}$	$25.77^{+1.67}_{-1.86}$	$25.83^{+1.51}_{-1.86}$	$24.36^{+1.24}_{-2.26}$
$H_{L,\text{total}}$ (mag)	$22.53^{+1.27}_{-1.73}$	$22.16^{+1.44}_{-1.76}$	$22.30^{+1.22}_{-1.82}$	$20.84^{+1.16}_{-1.98}$
$\bar{K}_{L,\text{total}}$ (mag)	$22.10^{+1.21}_{-1.70}$	$21.73^{+1.38}_{-1.71}$	$21.87^{+1.18}_{-1.77}$	$20.43^{+1.14}_{-1.89}$
V_{Blend} (mag)	20.21 ± 0.03	20.21 ± 0.03	20.21 ± 0.03	20.21 ± 0.03
I_{Blend} (mag)	19.25 ± 0.01	19.25 ± 0.01	19.25 ± 0.01	19.25 ± 0.01
χ^2	10,856.4	10,840.9	10,861.2	10,842.7
$\Delta\chi^2$	15.5	...	20.3	1.8

extinction in front of the lens using the following equation:

$$A_{i,L} = \frac{1 - \exp[-D_L/h_{\text{dust}}]}{1 - \exp[-D_S/h_{\text{dust}}]} A_{i,S}, \quad (13)$$

where i corresponds to the observed wavelength band, $A_{i,L}$ is the total extinction in the i band of the lens, $A_{i,S}$ is the total extinction in the i band of the source, h_{dust} is the scale length of dust in the event direction, given by $h_{\text{dust}} = (0.1 \text{ kpc})/\sin|b|$ as a function of the Galactic latitude b of the event. We estimated A_H and A_K from A_V using the wavelength dependence of the extinction law in the direction of the Galactic center from Nishiyama et al. (2008).

Table 6 lists the estimated parameters: the distance from the Earth to the lens, D_L ; the lens host mass, $M_{L,H}$; the lens companion mass, $M_{L,C}$; the orbital radius projected to the observation plane, $a_{L,\perp}$; the expected orbital radius, $a_{L,\text{exp}}$; the magnitudes with the extinction in the four wavelength bands $V_{L,j}$, $I_{L,j}$, $H_{L,j}$, and $K_{L,j}$ where j is ‘‘H’’ for the lens host, ‘‘C’’ for the lens companion, and ‘‘total’’ for the host and companion combined; and the magnitudes of the blends in the V and I bands, which are the upper limits of brightness in the lens system, V_{blend} and I_{blend} . Figures 6 and 7 show the posterior probability distributions for XLclose2 and XLwide2, respectively. The distribution of XLclose2 indicates an M-type or K-type stellar binary with a projected orbital radius $a_{L,\perp} = 0.13^{+0.02}_{-0.02}$ au located $7.2^{+1.1}_{-1.2}$ kpc from the Earth. The

distribution of XLwide2 also indicates an M-type or K-type stellar binary with a projected orbital radius $a_{L,\perp} = 34.74^{+7.51}_{-7.69}$ au located $7.1^{+1.0}_{-1.2}$ kpc from the Earth. Comparing the properties of the lens systems of the four models listed in Table 6, while the parameters related to the companion differ significantly among the models, they are consistent in the stellar type and the distance from the Earth.

As described in Section 5, the apparent magnitude of the source for XLclose2 is $(H_S, K_S) = (18.52 \pm 0.49, 18.29 \pm 0.48)$. The apparent magnitude for the lens host and lens companion combined is $(H_{L,\text{total}}, K_{L,\text{total}}) = (22.16 \pm 1.16, 21.73 \pm 1.55)$. Therefore, XLclose2 has a contrast between the apparent lens brightness and the apparent source brightness, which is 3.6 ± 1.7 mag in the H band and 3.4 ± 1.6 mag in the K band. The XLclose1 and XLwide1 models also have similar contrast to XLclose2. On the other hand, the contrast between the apparent lens brightness and the apparent source brightness in the XLwide2 model is 2.3 ± 1.6 in the H band and 2.1 ± 1.6 in the K band, slightly lower contrast than that in XLclose2.

7. Discussion and Conclusion

We performed a detailed analysis of the planetary microlensing candidate, OGLE-2019-BLG-0825. We first found that there are systematic residuals with the best-fit standard binary model with planetary mass ratio $q \sim 10^{-3}$. Therefore, we examined various combinations of possible higher-order effects. As a result, we found that models that include the xallarap effect can fit the residuals significantly better than models that do not.

Our Bayesian analysis for the best model XLclose2 estimated the lens host mass to be $0.25^{+0.29}_{-0.13} M_\odot$ and the lens system to be located $7.24^{+1.09}_{-1.17}$ kpc from Earth. For XLwide2, which is the best solution at $s > 1$, the lensing host is $0.37^{+0.32}_{-0.19} M_\odot$, and the lens system is estimated to be located $7.12^{+1.05}_{-1.22}$ kpc from Earth. Owing to degenerate solutions with various combinations of (q, s) values, the uncertainties in the mass and orbital radius of the lens companion are large. Since the relative proper motion between the lens and the source is about 1 mas yr^{-1} and the apparent magnitude contrast is large, it will be more than 30 years before the source and lens can be observed separately with the current high-resolution imaging instruments. In adaptive optics observations by The European Extremely Large Telescope, the FWHM is expected to reach 10 mas in the H band and 14 mas in the K band (Ryu et al. 2022). Therefore, it may be possible to observe the source and lens separately by mid-2030. It is unlikely that the degeneracy of the models will be resolved by follow-up observations because the proper motion and brightness of the lens system are comparable across models, but it may constrain the uncertainty in the lens system properties somewhat.

Calculations applying the assumption of $D_S = 8.0 \pm 1.4$ kpc and the isochrone model with age 10 Gyr in solar metallicity to the source show that the source companion OGLE-2019-BLG-0825Sb in the best 2L1S + xallarap model has a semimajor axis of 0.0594 ± 0.0005 au and an orbital period of 5.53 ± 0.05 days with mass $0.048 \pm 0.004 M_\odot$ orbiting the host source star OGLE-2019-BLG-0825S. The mass of the source companion is about that of a brown dwarf. The I -band luminosity ratio of the companion to the host is $L_{S,C}/L_{S,H} = (1.0 \pm 0.3) \times 10^{-7}$, which is faint and consistent with this analysis where the magnified flux of the second source is too weak to be detected.

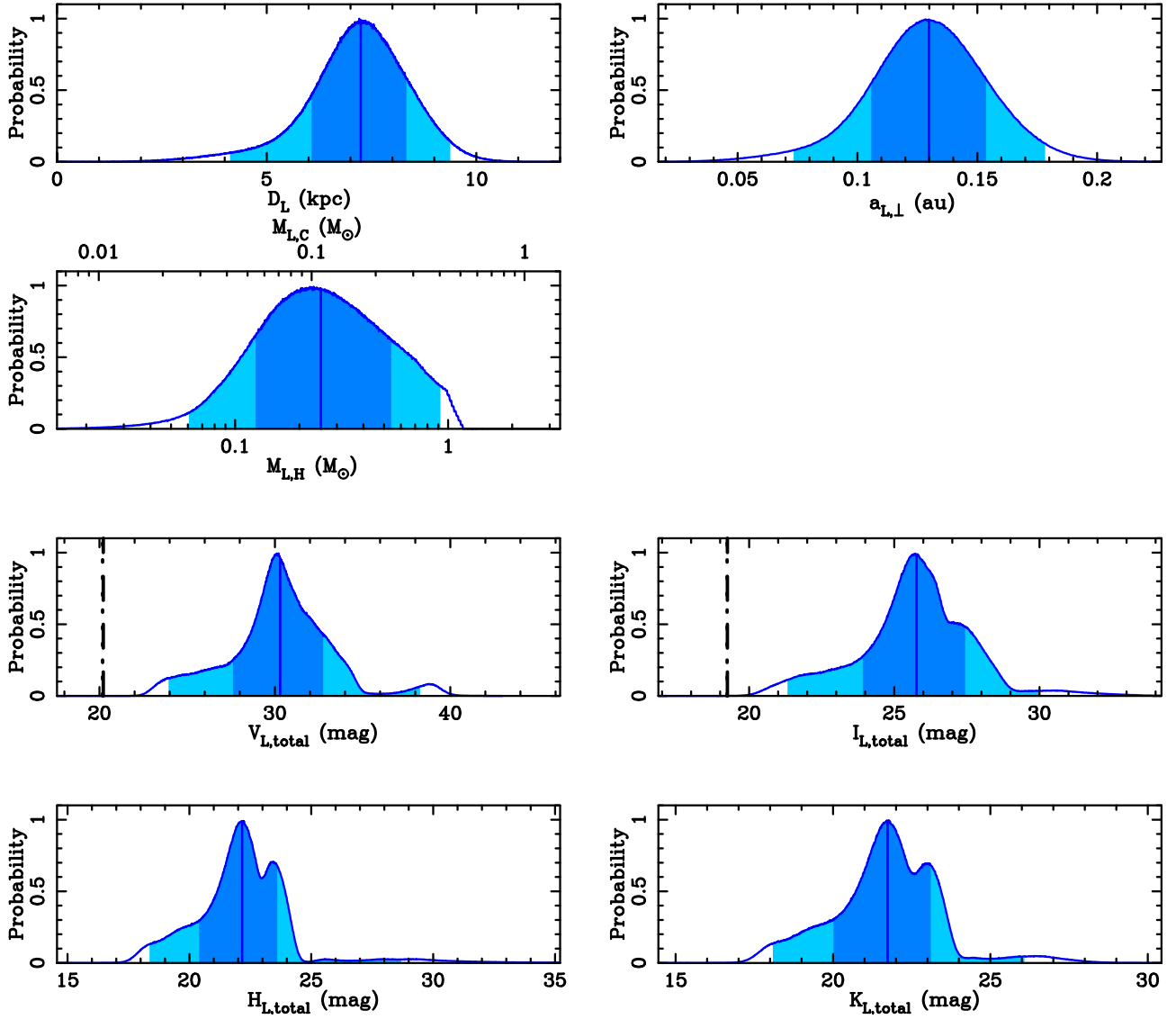


Figure 6. Posterior probability distribution of the properties of the lens system by Bayesian analysis for XLclose2. In each panel, the dark blue region indicates the 68.3% credible interval, the light blue region indicates the 95.4% credible interval, and the blue vertical line indicates the median value. The dashed lines at the left end of the panel of apparent V - and I -band magnitudes with extinction are the blending magnitudes obtained from light-curve modeling and are considered as the upper limit of brightness of the lens system.

We note that these properties of the source system are almost the same among the various models considered, even though the parameters of the lens system change.

We considered whether a variable source star could also explain the luminosity variations of this event over ~ 5 days without using the xallarap effect. Most of Classical Cepheids have pulsation periods ranging from about 1 to 100 days, and the longest period ones being rare, with a pulsation amplitude in the I band of 0.05–1 mag (Klagyivik & Szabados 2009), and the following period–luminosity relations (Gaia Collaboration et al. 2017):

$$M_I = -2.98 \log P - (1.28 \pm 0.08); \sigma_{\text{rms}} = 0.78, \quad (14)$$

where σ_{rms} is the variance around the periodic luminosity relation. At a pulsation period $P = 5.50 \pm 0.05$ days, the absolute magnitude of a type I Cepheid would be $M_I = -3.48 \pm 0.08$ mag. However our estimated absolute magnitude is $M_I = 4.5 \pm 0.4$ mag, which is too faint for a

classical Cepheid (see Table 5). Type II Cepheids have a pulsation period of about 1–50 days, with a pulsation amplitude of 0.3–1.2 mag, and the following period–luminosity relations (Ngeow et al. 2022):

$$M_I = -(2.09 \pm 0.08) \log P - (0.39 \pm 0.08); \sigma_{\text{rms}} = 0.24. \quad (15)$$

For a pulsation period $P = 5.50 \pm 0.05$ days, the absolute magnitude of a type II Cepheid would be $M_I = -1.94 \pm 0.13$ mag, which is also not plausible. RR Lyrae variables have color magnitudes close to those of main-sequence stars, but have a pulsation period of less than one day (e.g., Soszyński et al. 2009). Delta Scuti variables have a pulsation period of 0.01–0.2 days, and Gamma Doradus variables have a pulsation period of 0.3–2.6 days, both shorter than the xallarap signal of 5 days, and the spectral type is A–F, which is blue compared to the color of the source of this event. Furthermore, as described in Section 4.3, we performed a fitting with a model with variable source flux, using

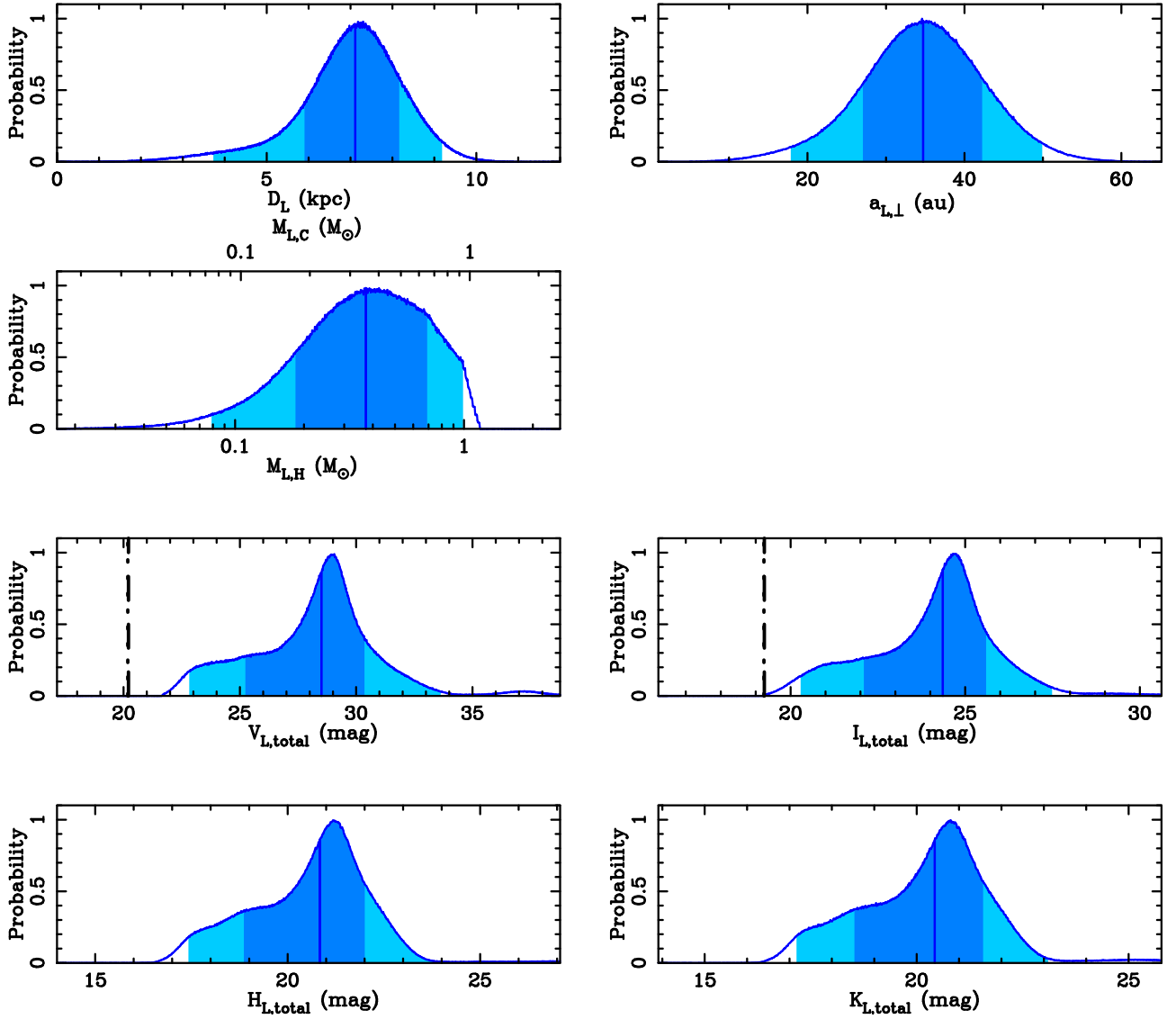


Figure 7. Same as Figure 6, but for XLwide2.

the best standard 2L1S model (i.e., close1). However, the improvement from the best standard 2L1S model was only 139.1, $\Delta\chi^2 = 764.6$ worse than the 2L1S + xallarap model. Therefore, we conclude that it is difficult to explain the xallarap signal assuming a variable source star. Note that although the conclusion is that the source of this event is not a variable star, many variable stars in the direction of the Galactic bulge have been discovered (e.g., Soszyński et al. 2011a,b; Iwanek et al. 2019), and there is a possibility that a candidate planetary microlensing event with a variable source will be observed in the future.

For the lens system, the inclusion of the xallarap effect significantly changed the $\Delta\chi^2$ plane of the mass ratio q versus separation s . The mass ratio of the best model was $q = (3.3 \pm 0.1) \times 10^{-3}$ without accounting for a xallarap effect, but became $q = (4.4 \pm 1.1) \times 10^{-1}$ with the xallarap effect. Furthermore, degenerate solutions with various combinations of (q, s) values were found within a small range of $\Delta\chi^2 \lesssim 10$. This event is the first case in which the short-period xallarap effect significantly affects the binary-lens parameters q and s . This effect is most likely to be seen in events with a caustic or cusp approach and no clear sharp caustic crossing. In events with a clear sharp

caustic crossing, this effect is not significant because the mass ratio q and separation s can be constrained from the caustic shape.

Although the xallarap effect has been examined in the past (e.g., Bennett et al. 2008; Sumi et al. 2010), few events have been able to eliminate possibilities of systematic errors and clearly identify the xallarap signal. Miyazaki et al. (2020) analyzed the planetary microlensing event OGLE-2013-BLG-0911 and found a significant xallarap signal. They conclude from the fitting parameters that the source companion, OGLE-2013-BLG-0911Sb has a mass $M_{S,C} = 0.14 \pm 0.02 M_\odot$, an orbital period $P_\xi = 36.7 \pm 0.8$ days, and a semimajor axis $a_S = 0.225 \pm 0.004$ au. However, they assume $M_{S,H} = 1 M_\odot$ and $D_S = 8$ kpc. Recently Rota et al. (2021) analyzed the candidate planetary event MOA-2006-BLG-074 and detected a xallarap effect. They estimated the source host's mass $M_{S,H} = 1.32 \pm 0.36 M_\odot$ from the color and magnitude of the source and found that the companion with mass $M_{S,C} = 0.44 \pm 0.14 M_\odot$ is orbiting the source host with orbital period $P_\xi = 14.2 \pm 0.2$ days and semimajor axis $a_S = 0.043 \pm 0.012$ au. The OGLE-2019-BLG-0825 event in this work is the second case after the MOA-2006-BLG-074 event (Rota et al. 2021) in which the physical properties

of a source system were estimated from the color and magnitude of the source. This event will be a valuable example for future xallarap microlensing analyses.

Rahvar & Dominik (2009) suggested that planets orbiting sources in the Galactic bulge could be detected by the xallarap effect with sufficiently good photometry. The fraction of close binaries like OGLE-2013-BLG-0911Sb is known to be anticorrelated with metallicity (Moe et al. 2019). The Galactic bulge observed in microlensing surveys suggests the presence of supersolar, solar, and low-metallicity components with $[\text{Fe}/\text{H}] \sim 0.32$, $[\text{Fe}/\text{H}] \sim 0.00$, and $[\text{Fe}/\text{H}] \sim -0.46$, respectively (García Pérez et al. 2018). Moe et al. (2019) reported that the fraction of close binaries, F_{close} , with separation $a < 10$ au is $F_{\text{close}} = 24\% \pm 4\%$ at $[\text{Fe}/\text{H}] = -0.2$ and $F_{\text{close}} = 10\% \pm 3\%$ at $[\text{Fe}/\text{H}] = 0.5$. However, the occurrence ratio of a companion with an orbit even shorter than ~ 0.5 au, to which the xallarap effect has sensitivity, is poorly understood.

Tokovinin et al. (2006) found that $\sim 68\%$ of close binary systems in the solar neighborhood with orbital period $P = 3\text{--}6$ days have an outer tertiary companion. Eggleton & Kiseleva-Eggleton (2006) and Fabrycky & Tremaine (2007) showed that Kozai–Lidov cycles with tidal friction (KCTF; Kiseleva et al. 1998; Eggleton & Kiseleva-Eggleton 2001) produce such very close binaries. First, in the KCTF, the inner companion’s eccentricity is increased by perturbations from the outer tertiaries. The inner companion in the eccentric orbit undergoes tidal friction near the periastron, and the orbit of the inner companion is finally circularized. Timescale equations for tidal circularization have been studied (e.g., Adams & Laughlin 2006; Correia et al. 2020). Because of their small radius relative to their mass the orbits of brown dwarfs are expected to take longer to circularize than those for Jupiter-like planets with the same orbital period over the gigayear scale. However, this is difficult to estimate because the tidal quality factor for brown dwarfs is not well constrained (Heller et al. 2010; Beatty et al. 2018). Meanwhile, Meibom & Mathieu (2005) demonstrated from the distribution of orbital eccentricity versus orbital period that most of the companions are circularized when the orbital period is shorter than ~ 15 days for the companions of halo stars and ~ 10 days for the companions of nearby G-type primaries. Therefore, in this analysis of OGLE-2019-BLG-0825, the source orbital eccentricity was fixed to $e_{\xi} = 0$. We also performed an analysis with free eccentricity, but our results were almost the same, and the improvement in χ^2 was only $\Delta\chi^2 \sim 16$, despite two additional parameters, e_{ξ} and T_{peri} .

Disk fragmentation and migration are also possible formation processes for close binaries. Moe & Kratter (2018) noted that the close binary fractions of solar-mass, pre-main-sequence binaries and field main-sequence binaries are almost identical (Mathieu 1994; Melo 2003), and concluded that majority of very close binaries with semimajor axis $a < 0.1$ au migrated when there was still gas in the circumstellar disk. Furthermore, Moe et al. (2019) showed that 90% of close binary stars with $a < 10$ au are the product of disk fragmentation. Tokovinin & Moe (2020) use simulations of disk fragmentation to show that the companion has difficulty migrating to $P < 100$ days without undergoing accretion that would grow it to more than $0.08 M_{\odot}$, explaining brown dwarf deserts.

The source companion OGLE-2019-BLG-0825Sb is the least massive source companion found in a xallarap event, and our favored interpretation is that it has a brown dwarf mass. The occurrence rate for brown dwarfs orbiting main-sequence

stars has been found to be low, less than 1% (Marcy & Butler 2000; Grether & Lineweaver 2006; Sahlmann et al. 2011; Santerne et al. 2016; Grieves et al. 2017). Fewer than 100 brown dwarf companions have been found in solar-type stars (e.g., Ma & Ge 2014; Grieves et al. 2017). There is a particularly dry region at orbital period $P < 100$ days (e.g., Kiefer et al. 2019, 2021). Therefore, if OGLE-2019-BLG-0825Sb is a short-period brown dwarf, it is a resident of the driest region of the brown dwarf desert, making it a very valuable sample for studying brown dwarf formation. Miyazaki et al. (2021) estimated the planetary yield detected by the Nancy Grace Roman Space Telescope (Spergel et al. 2015, previously named WFIRST, hereafter Roman) via xallarap signals assuming a planetary distribution of masses and orbital periods of Cumming et al. (2008). They predicted that Roman will characterize tens of short-period companions with the mass of a Jupiter or brown dwarf such as OGLE-2019-BLG-0825S. By comparing the predictions with the actual results, it will be possible to verify the brown dwarf desert in the Galactic bulge.

In this study, we assumed $D_S = 8.0 \pm 1.4$ kpc. Roman observations may be able to measure D_S by directly measuring astrometric parallax for bright source events (Gould et al. 2015). Even for non-bright source events, D_S can be determined by measuring the lensing flux F_L , π_E , and θ_E . Events with photometric accuracy ≤ 0.01 mag have been analytically shown to have the potential to measure θ_E with $\leq 10\%$ accuracy via astrometric microlensing observations in space (Gould & Yee 2014). Future observations of the xallarap effect may reveal the distribution of short-period binary stars in the Galactic center, which are usually difficult to observe.

Acknowledgments

We would appreciate Kento Masuda for valuable comments and discussions. Y.K.S. acknowledges the financial support from the Hayakawa Satio Fund awarded by the Astronomical Society of Japan. Work by N.K. is supported by the JSPS overseas research fellowship. The MOA project is supported by JSPS KAKENHI grant No. JSPS24253004, JSPS26247023, JSPS23340064, JSPS15H00781, JP16H06287, and JP17H02871. This research has made use of the KMTNet system operated by the Korea Astronomy and Space Science Institute (KASI) and the data were obtained at three host sites of CTIO in Chile, SAAO in South Africa, and SSO in Australia. Y.S. acknowledges support from BSF grant No. 2020740. J.C.Y. acknowledges support from U.S. NSF grant No. AST-2108414. U.G.J., N.B.-M., and J.S. acknowledge funding from the European Union H2020-MSCA-ITN-2019 under grant No. 860470 (CHAMELEON), from the Novo Nordisk Foundation Interdisciplinary Synergy Program grant No. NNF19OC0057374, and from the Carlsberg Foundation under grant No. CF18-0552. N.P.’s work was supported by Fundação para a Ciência e a Tecnologia (FCT) through the research grants UIDB/04434/2020 and UIDP/04434/2020. P.L.P. was partly funded by “Programa de Iniciación en Investigación-Universidad de Antofagasta INI-17-03.” G.D. acknowledges support by ANID, BASAL, FB210003.

ORCID iDs

Yuki K. Satoh  <https://orcid.org/0000-0002-1228-4122>
Naoki Koshimoto  <https://orcid.org/0000-0003-2302-9562>
David P. Bennett  <https://orcid.org/0000-0001-8043-8413>

Takahiro Sumi  <https://orcid.org/0000-0002-4035-5012>
 Nicholas J. Rattenbury  <https://orcid.org/0000-0001-5069-319X>
 Daisuke Suzuki  <https://orcid.org/0000-0002-5843-9433>
 Shota Miyazaki  <https://orcid.org/0000-0001-9818-1513>
 Andrzej Udalski  <https://orcid.org/0000-0001-5207-5619>
 Valerio Bozza  <https://orcid.org/0000-0003-4590-0136>
 Martin Dominik  <https://orcid.org/0000-0002-3202-0343>
 Yuki Hirao  <https://orcid.org/0000-0003-4776-8618>
 Iona Kondo  <https://orcid.org/0000-0002-3401-1029>
 Richard Barry  <https://orcid.org/0000-0003-4916-0892>
 Akihiko Fukui  <https://orcid.org/0000-0002-4909-5763>
 Stela Ishitani Silva  <https://orcid.org/0000-0003-2267-1246>
 Yoshitaka Itow  <https://orcid.org/0000-0002-8198-1968>
 Yutaka Matsubara  <https://orcid.org/0000-0002-9629-4810>
 Yasushi Muraki  <https://orcid.org/0000-0003-1978-2092>
 Greg Olmschenk  <https://orcid.org/0000-0001-8472-2219>
 Clément Ranc  <https://orcid.org/0000-0003-2388-4534>
 Aikaterini Vandroou  <https://orcid.org/0000-0002-9881-4760>
 Przemek Mróz  <https://orcid.org/0000-0001-7016-1692>
 Radosław Poleski  <https://orcid.org/0000-0002-9245-6368>
 Jan Skowron  <https://orcid.org/0000-0002-2335-1730>
 Michał K. Szymański  <https://orcid.org/0000-0002-0548-8995>
 Igor Soszyński  <https://orcid.org/0000-0002-7777-0842>
 Paweł Pietrukowicz  <https://orcid.org/0000-0002-2339-5899>
 Szymon Kozłowski  <https://orcid.org/0000-0003-4084-880X>
 Krzysztof Ulaczyk  <https://orcid.org/0000-0001-6364-408X>
 Krzysztof A. Rybicki  <https://orcid.org/0000-0002-9326-9329>
 Patryk Iwanek  <https://orcid.org/0000-0002-6212-7221>
 Marcin Wrona  <https://orcid.org/0000-0002-3051-274X>
 Mariusz Gromadzki  <https://orcid.org/0000-0002-1650-1518>
 Michael D. Albrow  <https://orcid.org/0000-0003-3316-4012>
 Sun-Ju Chung  <https://orcid.org/0000-0001-6285-4528>
 Cheongho Han  <https://orcid.org/0000-0002-2641-9964>
 Kyu-Ha Hwang  <https://orcid.org/0000-0002-9241-4117>
 Yoon-Hyun Ryu  <https://orcid.org/0000-0001-9823-2907>
 In-Gu Shin  <https://orcid.org/0000-0002-4355-9838>
 Yossi Shvartzvald  <https://orcid.org/0000-0003-1525-5041>
 Hongjing Yang  <https://orcid.org/0000-0003-0626-8465>
 Jennifer C. Yee  <https://orcid.org/0000-0001-9481-7123>
 Weicheng Zang  <https://orcid.org/0000-0001-6000-3463>
 Seung-Lee Kim  <https://orcid.org/0000-0003-0562-5643>
 Chung-Uk Lee  <https://orcid.org/0000-0003-0043-3925>
 Byeong-Gon Park  <https://orcid.org/0000-0002-6982-7722>
 Richard W. Pogge  <https://orcid.org/0000-0003-1435-3053>
 Uffe G. Jørgensen  <https://orcid.org/0000-0001-7303-914X>
 Sedighe Sajadian  <https://orcid.org/0000-0002-2859-1071>
 Jesper Skottfelt  <https://orcid.org/0000-0003-1310-8283>
 Colin Snodgrass  <https://orcid.org/0000-0001-9328-2905>
 Jeremy Tregloan-Reed  <https://orcid.org/0000-0002-9024-4185>
 Nanna Bach-Møller  <https://orcid.org/0000-0002-8799-0080>
 Martin Burgdorf  <https://orcid.org/0000-0002-5854-4217>
 Giuseppe D'Ago  <https://orcid.org/0000-0001-9697-7331>
 Lauri Haikala  <https://orcid.org/0000-0001-9279-2815>
 James Hitchcock  <https://orcid.org/0000-0002-1508-2243>
 Markus Hundertmark  <https://orcid.org/0000-0003-0961-5231>

Nuno Peixinho  <https://orcid.org/0000-0002-6830-476X>
 Sohrab Rahvar  <https://orcid.org/0000-0002-7084-5725>
 John Southworth  <https://orcid.org/0000-0002-3807-3198>

References

- Adams, F. C., & Laughlin, G. 2006, *ApJ*, 649, 1004
 Alard, C. 2000, *A&AS*, 144, 363
 Alard, C., & Lupton, R. H. 1998, *ApJ*, 503, 325
 Albrow, M. D., Horne, K., Bramich, D. M., et al. 2009, *MNRAS*, 397, 2099
 Badenes, C., Mazzola, C., Thompson, T. A., et al. 2018, *ApJ*, 854, 147
 Baraffe, I., Chabrier, G., Barman, T. S., Allard, F., & Hauschildt, P. H. 2003, *A&A*, 402, 701
 Beatty, T. G., Morley, C. V., Curtis, J. L., et al. 2018, *AJ*, 156, 168
 Beaulieu, J. P., Bennett, D. P., Fouqué, P., et al. 2006, *Natur*, 439, 437
 Bennett, D. P. 2010, *ApJ*, 716, 1408
 Bennett, D. P., Bhattacharya, A., Anderson, J., et al. 2015, *ApJ*, 808, 169
 Bennett, D. P., Bond, I. A., Udalski, A., et al. 2008, *ApJ*, 684, 663
 Bennett, D. P., & Rhie, S. H. 1996, *ApJ*, 472, 660
 Bensby, T., Yee, J. C., Feltzing, S., et al. 2013, *A&A*, 549, A147
 Bond, I. A., Abe, F., Dodd, R. J., et al. 2001, *MNRAS*, 327, 868
 Boyajian, T. S., van Belle, G., & von Braun, K. 2014, *AJ*, 147, 47
 Bramich, D. M. 2008, *MNRAS*, 386, L77
 Bramich, D. M., Horne, K., Albrow, M. D., et al. 2013, *MNRAS*, 428, 2275
 Bressan, A., Marigo, P., Girardi, L., et al. 2012, *MNRAS*, 427, 127
 Claret, A., & Bloemen, S. 2011, *A&A*, 529, A75
 Correia, A. C. M., Bourrier, V., & Delisle, J. B. 2020, *A&A*, 635, A37
 Cumming, A., Butler, R. P., Marcy, G. W., et al. 2008, *PASP*, 120, 531
 Delfosse, X., Forveille, T., Ségransan, D., et al. 2000, *A&A*, 364, 217
 Dominik, M., Jørgensen, U. G., Rattenbury, N. J., et al. 2010, *AN*, 331, 671
 Dong, S., Gould, A., Udalski, A., et al. 2009, *ApJ*, 695, 970
 Eggleton, P. P., & Kiseleva-Eggleton, L. 2001, *ApJ*, 562, 1012
 Eggleton, P. P., & Kiseleva-Eggleton, L. 2006, *Ap&SS*, 304, 75
 Fabrycky, D., & Tremaine, S. 2007, *ApJ*, 669, 1298
 Fressin, F., Torres, G., Charbonneau, D., et al. 2013, *ApJ*, 766, 81
 Fukui, A., Gould, A., Sumi, T., et al. 2015, *ApJ*, 809, 74
 Gaia Collaboration, Clementini, G., Eyer, L., et al. 2017, *A&A*, 605, A79
 García Pérez, A. E., Ness, M., Robin, A. C., et al. 2018, *ApJ*, 852, 91
 Gaudi, B. S. 2012, *ARA&A*, 50, 411
 Gonzalez, G., Brownlee, D., & Ward, P. 2001, *Icar*, 152, 185
 González Hernández, J. I., & Bonifacio, P. 2009, *A&A*, 497, 497
 Gould, A. 1992, *ApJ*, 392, 442
 Gould, A. 2000, *ApJ*, 542, 785
 Gould, A. 2004, *ApJ*, 606, 319
 Gould, A., Huber, D., Penny, M., & Stello, D. 2015, *JKAS*, 48, 93
 Gould, A., & Loeb, A. 1992, *ApJ*, 396, 104
 Gould, A., Udalski, A., An, D., et al. 2006, *ApJL*, 644, L37
 Gould, A., & Yee, J. C. 2014, *ApJ*, 784, 64
 Grether, D., & Lineweaver, C. H. 2006, *ApJ*, 640, 1051
 Griest, K., & Hu, W. 1992, *ApJ*, 397, 362
 Grieves, N., Ge, J., Thomas, N., et al. 2017, *MNRAS*, 467, 4264
 Han, C., & Gould, A. 1995, *ApJ*, 447, 53
 Han, C., & Gould, A. 1997, *ApJ*, 480, 196
 Heller, R., Jackson, B., Barnes, R., Greenberg, R., & Homeier, D. 2010, *A&A*, 514, A22
 Henry, T. J., & McCarthy, D. W. J. 1993, *AJ*, 106, 773
 Hirsch, L. A., Rosenthal, L., Fulton, B. J., et al. 2021, *AJ*, 161, 134
 Holtzman, J. A., Watson, A. M., Baum, W. A., et al. 1998, *AJ*, 115, 1946
 Howard, A. W., Marcy, G. W., Bryson, S. T., et al. 2012, *ApJS*, 201, 15
 Ida, S., & Lin, D. N. C. 2004, *ApJ*, 616, 567
 Iwanek, P., Soszyński, I., Skowron, J., et al. 2019, *ApJ*, 879, 114
 Kennedy, G. M., Kenyon, S. J., & Bromley, B. C. 2006, *ApJL*, 650, L139
 Kiefer, F., Hébrard, G., Lecavelier des Etangs, A., et al. 2021, *A&A*, 645, A7
 Kiefer, F., Hébrard, G., Sahlmann, J., et al. 2019, *A&A*, 631, A125
 Kim, D. J., Kim, H. W., Hwang, K. H., et al. 2018, *AJ*, 155, 76
 Kim, S.-L., Lee, C.-U., Park, B.-G., et al. 2016, *JKAS*, 49, 37
 Kiseleva, L. G., Eggleton, P. P., & Mikkola, S. 1998, *MNRAS*, 300, 292
 Klagyivik, P., & Szabados, L. 2009, *A&A*, 504, 959
 Koshimoto, N., Bennett, D. P., Suzuki, D., & Bond, I. A. 2021, *ApJL*, 918, L8
 Kroupa, P., & Tout, C. A. 1997, *MNRAS*, 287, 402
 Lada, C. J. 2006, *ApJL*, 640, L63
 Laughlin, G., Bodenheimer, P., & Adams, F. C. 2004, *ApJL*, 612, L73
 Liebes, S. 1964, *PhRv*, 133, 835
 Lineweaver, C. H., Fenner, Y., & Gibson, B. K. 2004, *Sci*, 303, 59

- Ma, B., & Ge, J. 2014, *MNRAS*, **439**, 2781
- Marcy, G. W., & Butler, R. P. 2000, *PASP*, **112**, 137
- Mathieu, R. D. 1994, *ARA&A*, **32**, 465
- Meibom, S., & Mathieu, R. D. 2005, in ASP Conf. Ser. 333, Tidal Evolution and Oscillations in Binary Stars, ed. A. Claret, A. Giménez, & J. P. Zahn (San Francisco, CA: ASP), 95
- Melo, C. H. F. 2003, *A&A*, **410**, 269
- Miyazaki, S., Johnson, S. A., Sumi, T., et al. 2021, *AJ*, **161**, 84
- Miyazaki, S., Sumi, T., Bennett, D. P., et al. 2020, *AJ*, **159**, 76
- Moe, M., & Kratter, K. M. 2018, *ApJ*, **854**, 44
- Moe, M., Kratter, K. M., & Badenes, C. 2019, *ApJ*, **875**, 61
- Mróz, P., Udalski, A., Skowron, J., et al. 2019, *ApJS*, **244**, 29
- Nataf, D. M., Gould, A., Fouqué, P., et al. 2013, *ApJ*, **769**, 88
- Ngeow, C.-C., Bhardwaj, A., Henderson, J.-Y., et al. 2022, *AJ*, **164**, 154
- Nishiyama, S., Nagata, T., Tamura, M., et al. 2008, *ApJ*, **680**, 1174
- Paczynski, B. 1986, *ApJ*, **304**, 1
- Paczynski, B. 1991, *ApJL*, **371**, L63
- Paczynski, B. 1997, arXiv:astro-ph/9711007
- Poindexter, S., Afonso, C., Bennett, D. P., et al. 2005, *ApJ*, **633**, 914
- Rahvar, S., & Dominik, M. 2009, *MNRAS*, **392**, 1193
- Ranc, C., Bennett, D. P., Hirao, Y., et al. 2019, *AJ*, **157**, 232
- Rhie, S. H., Becker, A. C., Bennett, D. P., et al. 1999, *ApJ*, **522**, 1037
- Rota, P., Hirao, Y., Bozza, V., et al. 2021, *AJ*, **162**, 59
- Ryu, Y.-H., Kil Jung, Y., Yang, H., et al. 2022, *AJ*, **164**, 180
- Sahlmann, J., Ségransan, D., Queloz, D., et al. 2011, *A&A*, **525**, A95
- Sako, T., Sekiguchi, T., Sasaki, M., et al. 2008, *ExA*, **22**, 51
- Santerne, A., Díaz, R. F., Moutou, C., et al. 2012, *A&A*, **545**, A76
- Santerne, A., Moutou, C., Tsantaki, M., et al. 2016, *A&A*, **587**, A64
- Sit, T., & Ness, M. K. 2020, *ApJ*, **900**, 4
- Smith, M. C., Mao, S., & Paczyński, B. 2003, *MNRAS*, **339**, 925
- Soszyński, I., Udalski, A., Szymański, M. K., et al. 2009, *AcA*, **59**, 1
- Soszyński, I., Dziembowski, W.A., & Udalski, A. 2011a, *AcA*, **61**, 1
- Soszyński, I., Udalski, A., Pietrukowicz, P., et al. 2011b, *AcA*, **61**, 285
- Spiegel, D., Gehrels, N., Baltay, C., et al. 2015, arXiv:1503.03757
- Spinelli, R., Ghirlanda, G., Haardt, F., Ghisellini, G., & Scuderi, G. 2021, *A&A*, **647**, A41
- Sumi, T., Abe, F., Bond, I. A., et al. 2003, *ApJ*, **591**, 204
- Sumi, T., Bennett, D. P., Bond, I. A., et al. 2010, *ApJ*, **710**, 1641
- Sumi, T., Kamiya, K., Bennett, D. P., et al. 2011, *Natur*, **473**, 349
- Szymański, M. K., Udalski, A., Soszyński, I., et al. 2011, *AcA*, **61**, 83
- Tokovinin, A., & Moe, M. 2020, *MNRAS*, **491**, 5158
- Tokovinin, A., Thomas, S., Sterzik, M., & Udry, S. 2006, *A&A*, **450**, 681
- Tomaney, A. B., & Crots, A. P. S. 1996, *AJ*, **112**, 2872
- Udalski, A. 2003, *AcA*, **53**, 291
- Udalski, A., Szymanski, M., Stanek, K. Z., et al. 1994, *AcA*, **44**, 165
- Udalski, A., Szymański, M. K., & Szymański, G. 2015, *AcA*, **65**, 1
- Wozniak, P. R. 2000, *AcA*, **50**, 421
- Yee, J. C., Gould, A., Beichman, C., et al. 2015, *ApJ*, **810**, 155
- Yee, J. C., Shvartzvald, Y., Gal-Yam, A., et al. 2012, *ApJ*, **755**, 102
- Zhu, W., Udalski, A., Novati, S. C., et al. 2017, *AJ*, **154**, 210